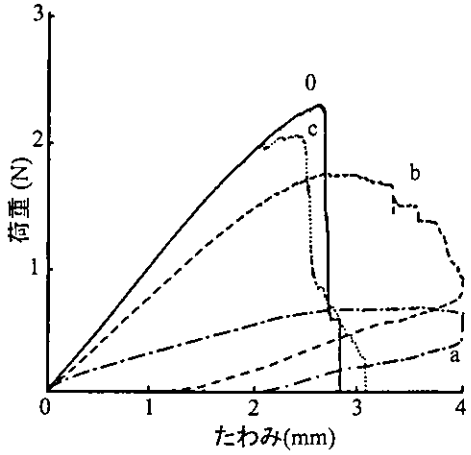

図 8　無処理 FRP ワイヤーの荷重－たわみ曲線の吸水，乾燥条件による変化
0：浸漬前，a：浸漬後，b：乾燥（23℃），c：乾燥（100℃）

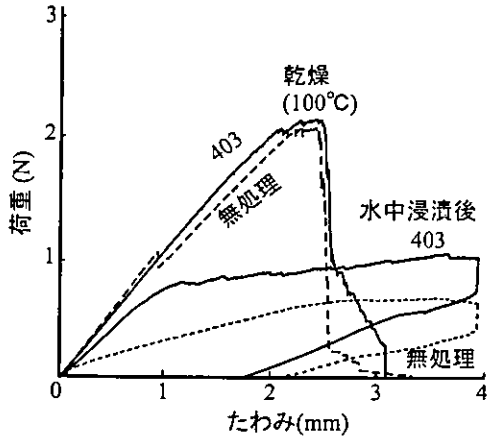

図 9　403 処理 FRP ワイヤーの荷重－たわみ曲線の吸水，乾燥条件による変化（無処理との比較）

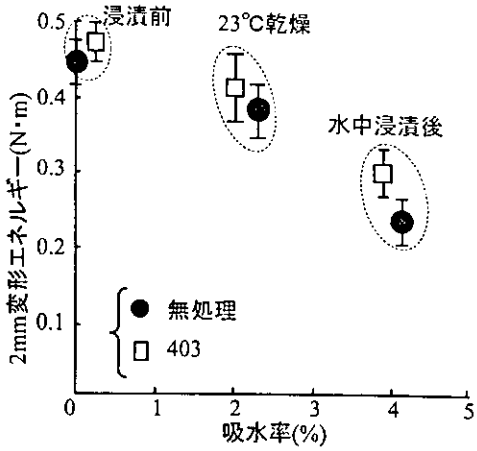

図 10　2 mm 変形エネルギーと吸水率の相関

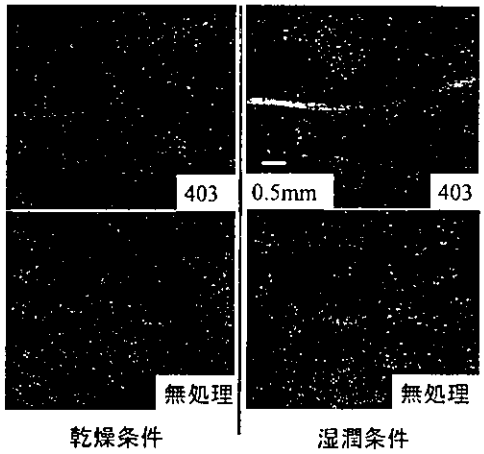

図 11　応力緩和試験直後の FRP ワイヤーの変形

れた．

(2)　403 ワイヤー

図 9 に 403 ワイヤーの浸漬直後と 100℃ 乾燥後の荷重－たわみ曲線を無処理ワイヤーと比較して示す．どちらのワイヤーも浸漬直後よりも 100℃ で 1 時間乾燥した後の勾配のほうが大きい．浸漬直後の 403 ワイヤーの勾配は無処理ワイヤーよりも大きいが，たわみ 1 mm あたりから鋸歯状の荷重低下を繰り返しながら荷重は緩やかに上昇した．しかし，100℃ で 1 時間乾燥すると，無処理ワイヤーとの明確な違いは見られなくなった．

(3)　2 mm 変形エネルギー

図 10 に 2 mm 変形エネルギーと吸水率の相関を示す．ここでは浸漬前の吸水率を 0% とした．水中浸漬後の無処理ワイヤーと 403 ワイヤー間にのみ有意差が認められた（$p<0.05$）．また，水中浸漬後は浸漬前および 23℃ 乾燥と比較して有意に低下した（$p<0.05$）．吸水率が高くなると 2 mm 変形エネルギーは小さくなった．

4.　応力緩和試験

1)　永 久 変 形

図 11 に試験直後のワイヤーを示す．乾燥条件下（左段）では両ワイヤーとも目視できるだけの永久変形は見られないが，湿潤条件下（右段）では永久変形が見られ，特に無処理ワイヤー（下段）には大きな変形が見られた．

2)　応力緩和と AE の発生

図 12 に荷重保持率の乾燥，湿潤条件およびカップリング処理の有無による変化を示す．乾燥条件下での 24 時間後の荷重保持率は両ワイヤーとも約 85% とほぼ同程度であったが，湿潤条件では 403 ワイヤーが約 43%，無処理ワイヤーは 14.5% まで低下した．

図 13 に乾燥条件での荷重保持率と AE の発生を示す．両ワイヤーとも荷重保持率の低下は少なく，AE の発生も散発的で少なかった．

図 14 に湿潤条件での荷重保持率と AE の発生を示す．

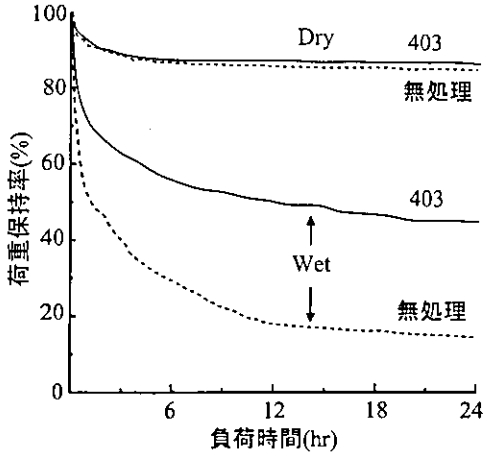

図 12　荷重保持率の乾燥，湿潤条件およびカップリング処理の有無による変化

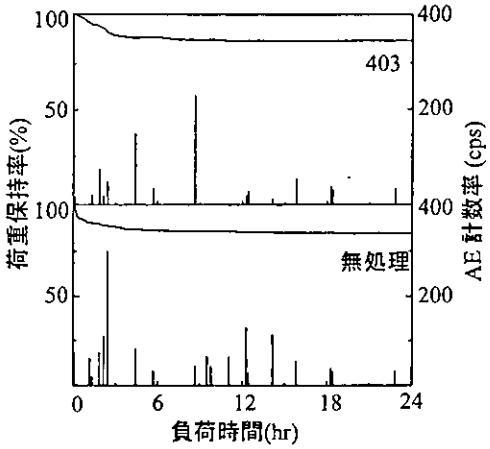

図 13　応力緩和試験と AE の発生（乾燥条件）

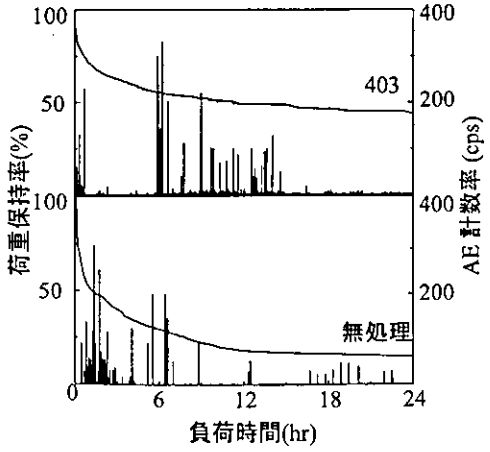

図 14　応力緩和試験と AE の発生（湿潤条件）

両ワイヤーとも荷重保持率の低下が見られるが，無処理ワイヤーは浸漬直後から大きく低下し AE が発生したのに対して，403 ワイヤーは無処理ワイヤーほど大きな低下はなく，AE も 6 時間付近から発生が増加した．

図 15 に図 13，14 の応力緩和試験中に発生した AE を

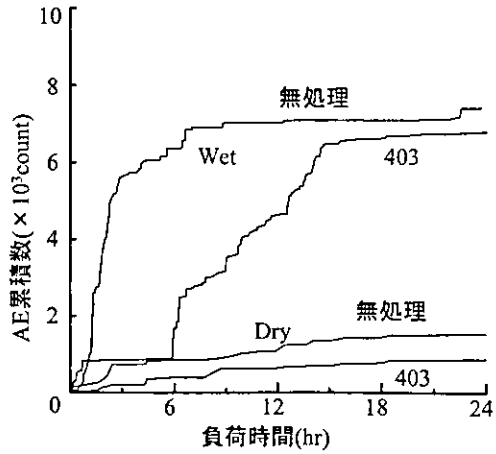

図 15　応力緩和試験における AE 計数の負荷時間に伴う変化

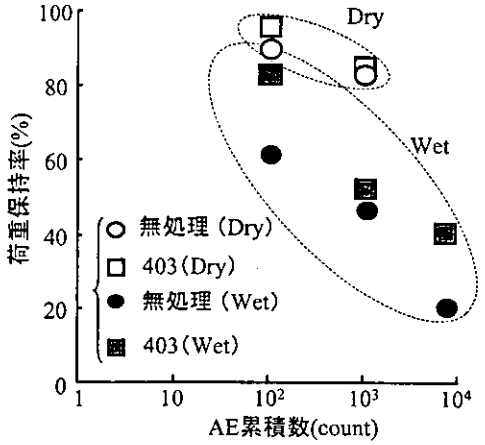

図 16　荷重保持率と AE 累積数との相関

経時的に積算した AE 累積数を示す．乾燥条件では両ワイヤーとも緩やかに増加し，24 時間後には無処理では約 1500，403 ワイヤー では約 800count に達した．湿潤条件において無処理ワイヤーでは浸漬直後から急増するのに対し 403 ワイヤーでは 6 時間後から急増し，24 時間後には両ワイヤーとも乾燥条件の約 5～9 倍である約 7000count の AE が発生した．

図 16 に荷重保持率と AE 累積数の相関を示す．すべての条件で AE 累積数の増加とともに荷重保持率は低下した．同じ AE 累積数であれば，乾燥条件より湿潤条件のほうが，また 403 ワイヤーより無処理ワイヤーのほうが荷重保持率は低い値を示した．

5.　定たわみ曲げ試験

1)　FRP ワイヤーの視覚的変化

図 3 右に定たわみ曲げ試験後のワイヤーを示す．乾燥条件では目視できるほどの永久変形は見られないが，湿潤条件（水中浸漬 24 時間後）では永久変形が見られ，特に無処理ワイヤーには大きな変形が見られた．

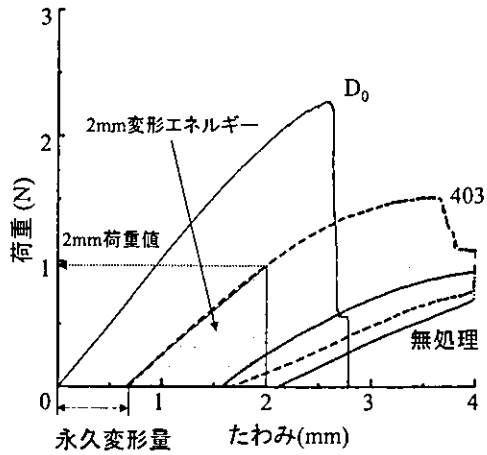

図 17　24 時間水中浸漬定たわみ曲げ変形後の荷重－たわみ曲線
曲げ変形前：D_0（無処理），変形後：403，無処理

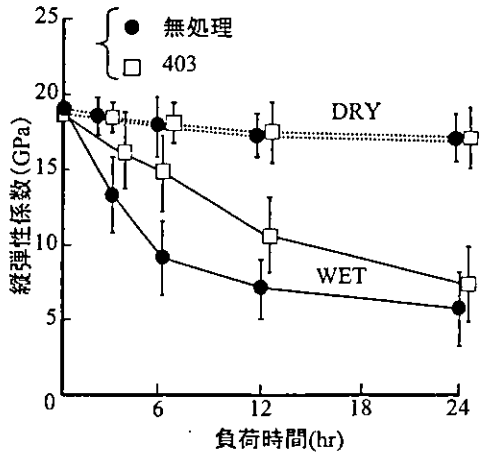

図 18　縦弾性係数の負荷時間による変化

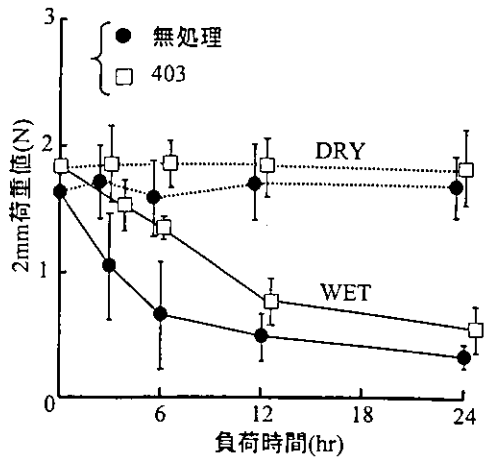

図 19　2 mm 荷重値の負荷時間による変化

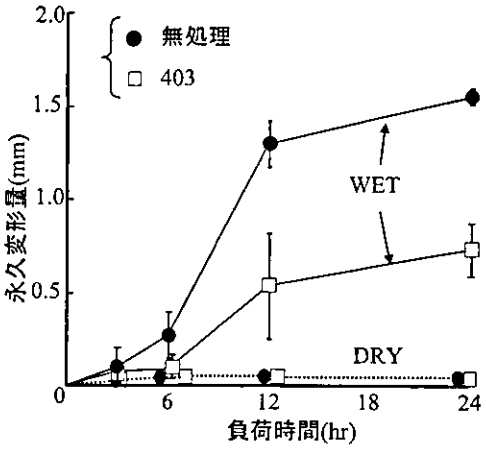

図 20　永久変形量の負荷時間による変化

2)　3 点曲げによる評価

図 17 に 24 時間水中浸漬定たわみ曲げ変形後の 3 点曲げ試験による荷重－たわみ曲線の代表例を示す．定たわみ曲げ変形により永久変形が生じた試験片に 3 点曲げを行うと，荷重が負荷し始めるロードセルの位置が永久変形量として示される．この永久変形量は 403 ワイヤー（図中 約 0.7 mm）よりも無処理ワイヤーのほうが大きく（図中 約 1.6 mm），また勾配は試験前 D_0（無処理ワイヤー）に比べ小さかった．

図中に 403 ワイヤーの 2 mm 荷重値，および 2 mm 変形エネルギーを示す．2 mm 荷重値はたわみ 2 mm である時の荷重値，2 mm 変形エネルギーはたわみ 2 mm までの荷重－たわみ曲線が囲む面積として求めたが，このたわみ 2 mm には 3 点曲げを行う前の定たわみ曲げ試験による永久変形量も含まれているため，実際たわんでいる量は 2 mm よりも小さいものとなる．永久変形量が小さく，勾配が大きい 403 ワイヤーの 2 mm 荷重値および 2 mm 変形エネルギーは，無処理ワイヤーより大きい値を示した．

(1)　縦弾性係数

図 18 に縦弾性係数の負荷時間による変化を示す．乾燥条件ではどの試験片においても約 19GPa と大きな低下は見られなかったが，湿潤条件では曲げ変形時間が長いものほど低下し，浸漬 24 時間後における縦弾性係数は，無処理ワイヤーで 19GPa から 8.5GPa へ，403 ワイヤーで 18GPa から 7.3GPa へと半分以下に低下した．また浸漬後 6 時間において 403 ワイヤーは無処理ワイヤーより有意に高い値を示した（$p<0.05$）が，12，24 時間後には有意差は認められなかった（$p>0.05$）．

(2)　2 mm 荷重値

図 19 に 2 mm 荷重値の負荷時間による変化を示す．乾燥条件ではどの試験片においても約 1.6～1.8N と大きな変化は見られなかったが，湿潤条件では曲げ変形時間が長いものほど低下し，浸漬 24 時間後における 2 mm 荷重値は，無処理ワイヤーで 1.6N から 0.3N へと約 1/5 に，403 ワイヤーで 1.8N から 0.6N へと約 1/3 に低下した．また浸漬後 6 時間において 403 ワイヤーは無処理ワイヤーより有意に高い値を示した（$p<0.01$）が，12，24 時間

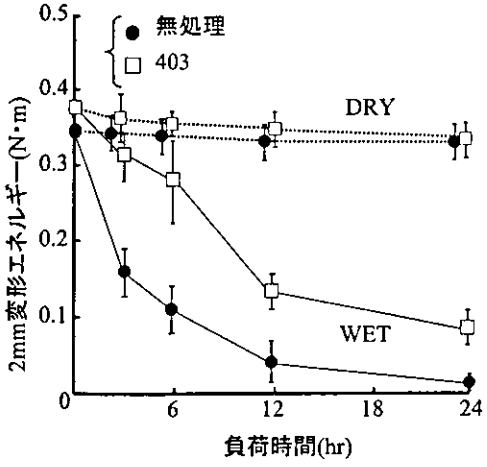

図21 2 mm 変形エネルギーの負荷時間による変化

後には有意差は認められなかった（$p>0.05$）.

(3) 永久変形量

図20に永久変形量の負荷時間による変化を示す.乾燥条件ではどの試験片においてもほとんど変形は見られなかったが，湿潤条件では曲げ変形時間が長いものほど変形量が増加し，特に無処理ワイヤーは約1.5 mmと403ワイヤーに比べて約2倍の変形が見られた.

(4) 2 mm 変形エネルギー

図21に2 mm変形エネルギーの負荷時間による変化を示す．乾燥条件ではどの試験片においてもその値に大きな変化は見られなかったが，湿潤条件では曲げ変形時間が長いものほど低下し，浸漬24時間後の403ワイヤーは0.39N・mから0.09N・mへと約1/4へ，無処理ワイヤーでは0.37N・mから0.012N・mへと約1/30に低下した.

考　　察

1. 水への感受性

始めに浸漬による機械的特性の劣化は水に特有なのか，有機溶媒のような他の液体でも劣化は起きるのか調べた．図5に示した荷重－たわみ曲線を比較すると，有機溶媒中に浸漬したワイヤーはほとんど劣化を起こしていない．FRPワイヤーの劣化の主たる原因は水にあることが確認された.

2. 各試験の意義

1) 吸水試験

マルチブラケット法の治療初期段階にはNi-Ti系ワイヤーが，治療中期から後期にかけてはCo-Crワイヤーが使用されることが多い．FRPワイヤーはその機械的特性から治療の中期以降に使用されることが想定される．その場合30日程度の期間，継続して口腔内で使用されることになるため，湿潤条件下での材料的特性についての検討が必要である．マトリックスとしてポリマーを使用するFRPワイヤーの吸水試験を行い，吸水動態と機械的特性に及ぼす吸水の影響を知ることは重要である．また，ガラス繊維の表面処理に使用したカップリング剤がマトリックスの吸水率に及ぼす影響を調べた.

図6に示したように，FRPワイヤーの吸水はおおよそ約3～6時間で終了している．無処理ワイヤーの吸水率は100%ポリマーワイヤーに比べ有意に高かった（$p<0.01$）．これは吸水によりガラス繊維/マトリックス間の界面剥離が進行したためと思われる．また浸漬後6時間での403ワイヤーは無処理ワイヤーより有意に低い（$p<0.05$）が，次第に差が小さくなった．これは浸漬後6時間を過ぎた頃に吸水が完了し，カップリング処理による界面接着効果が低下し，界面剥離が進行したためと考えられる.

2) 吸水－乾燥試験

FRPワイヤーの湿潤条件下における機械的特性低下の要因が吸水であるのか，また，その変化は可逆的なのか不可逆的か，さらに吸水率と機械的特性との関連を調べるために吸水－乾燥試験を行った．この試験では吸水率の増減にともなう荷重－たわみ曲線の変化を調べ，機械的特性と吸水率の関係を検証した．その結果，図9，10に示したように，吸水することで機械的特性が低下するが，乾燥により回復することがわかった．これは吸水により剥離したガラス繊維/マトリックス間の界面が，乾燥することで機械的な嵌合効力が働き，曲げ変形に対する抵抗として荷重を発揮したためと推測できる．また，100℃ 乾燥後のワイヤー重量が浸漬前より軽くなったのは未重合レジンの溶解も可能性として考えられるが，マトリックスの溶解率として換算すると約1%になり今後，さらに検討が必要である.

3) 応力緩和試験

マルチブラケットによる矯正治療の来院間隔は1ヵ月以上になることもあり，その期間中のワイヤーには変形や破断がなく，歯を移動させるのに十分な矯正力を保っていることが臨床応用するにあたって必要である．乾燥条件ならびに湿潤条件で応力緩和試験を行うことで，FRPワイヤーが持つ矯正力の時間による変化，および吸水による影響を評価した．乾燥条件では約6時間以降の荷重低下はほとんど見られないのに対して，湿潤条件では始めの3～6時間で急激に，その後は緩やかに荷重低下し続けた．これは，最初に吸水した外層部マトリックスの膨潤，界面の剥離が起こり，強い張力のかかっている外層部のガラス繊維が滑り出すためと推測できる.

4) AE測定

FRPワイヤーには応力の低下とともに試料内部で何らかの変化が起きているはずである．これまでは試験後の試料をSEM観察することでFRPワイヤーに起こった破壊を検証してきた．しかし，それは破壊プロセスの最終時点での状況であり，途中で起きているミクロな破壊プロセスについての情報は得られない.

アコースティック・エミッション（AE）は，“個体が変形あるいは破壊する際に，個体がそれまで蓄えていた

ひずみエネルギーを開放する結果として発生する弾性波" と定義されている．AE 法はこの弾性波を材料表面に設置した AE 変換子で検出し，信号処理をして，材料の微視的挙動の解明，構造物などの非破壊検査などに応用する技術である．AE 法は材料の欠陥自体が発するエネルギーを直接観測する手法であるので，図 13，14 に示したように塑性変形の微細な破壊過程をリアルタイムにモニターすることができ，発生した AE を累積することで図 15，16 に示したように破壊の進行状況や，微細な破壊が荷重に与える影響を検討することができた．

5)　定たわみ曲げ試験

臨床では治療の進行状況によって，前回の診療時に口腔内に装着されたワイヤーを再び装着することは少なくない．このときに再び発揮できる矯正力はワイヤーの耐久性を表す一つの指標であると考えた．本試験ではワイヤーにある期間一定のたわみを与え，除荷後 3 点曲げを行い，得られた荷重－たわみ曲線より縦弾性係数，永久変形量，2 mm 荷重値，2 mm 変形エネルギーを求め評価に用いた．また，応力緩和試験は 1 本の試料で試験機を長期間占有するため，まとまった本数の試験を行うには向いていない．今回，定たわみ曲げ試験機を用いることで大量の試験片を同一条件で試験することが可能となった．

6)　2 mm 変形エネルギーの意義

本研究では荷重－たわみ曲線から得られた指標が多く使われている．例えば水中浸漬定たわみ負荷後の機械的特性は永久変形量，縦弾性係数，2 mm 荷重値等で評価している．しかし縦弾性係数が同じであっても永久変形量が異なれば，2 mm 荷重値も異なってくる．同じように永久変形量が同じであっても縦弾性係数が異なれば 2 mm 荷重値は異なってくる．このように，1 つの指標だけで試験片の物性を包括的に表すことは必ずしも容易ではない．そこで機械的特性を総合的に 1 つの指標で表すものとして，たわみ 2 mm までの荷重－たわみ曲線下の面積を 2 mm 変形に要するエネルギーとして評価することを試みた．

3.　FRP ワイヤーの再使用について

定たわみ曲げ試験の結果に示すように，カップリング処理されているワイヤーであっても 6 時間以上使用された場合，永久変形が残り（図 20），2 mm 変形エネルギーも 24 時間後には約 1/4 に低下してしまう（図 21）．口腔内で 1 ヵ月使用されたアーチワイヤーの機械的特性の低下はさらに大きいと推測される．臨床において再度ブラケットスロットに挿入されても効率よく歯牙を動かすことは現段階では困難であると思われる．

4.　カップリング処理の効果

これまで FRP ワイヤーはマトリックスとしてポリメチルメタクリレート（PMMA），ウレタンジメタクリレート（UDMA）を用いてきた．これら有床義歯用材料や歯科充填用材料として広く使われているレジンには吸水性があることがすでに知られており，長期水中浸漬による材質劣化が指摘されている．PMMA，UDMA，Bis－GMA をマトリックスとした試験片を用いて，たわみ 2 mm，湿潤条件下での応力緩和試験では，UDMA ワイヤーは約 5 時間，PMMA ワイヤーは試験直後に破折したが Bis－GMA ワイヤーは 24 時間破折しなかった（未発表）．この結果より，最も耐久性が期待できる Bis－GMA を今回マトリックスに用いた．

図 10 の 2 mm 変形エネルギーと吸水率の相関から分かるように，吸水後の 403 ワイヤーは無処理ワイヤーに比べて 2 mm 変形エネルギーが有意に大きい値を示した（$p<0.05$）が，乾燥するにしたがって両ワイヤーとも機械的特性が回復し，差が小さくなった．吸水後のマトリックスは膨張し，ガラス繊維／マトリックス間の界面は剥離しやすくガラス繊維がマトリックスの中を滑りやすい状態であるが，403 ワイヤーには吸水後も界面接着効果が働き機械的特性をある程度保持し，違いが出たと推測できる．

吸水試験においては図 6 に示したように 3～6 時間で吸水がほぼ完了している．また図 12 に示したように湿潤条件での応力緩和試験においても荷重保持率が急激に低下するのはいずれも 3～6 時間までであることで一致しており，403 ワイヤーは無処理ワイヤーに比べ荷重を高く保持していた．

AE の発生については図 15 に示したように無処理ワイヤーは浸漬直後から，403 ワイヤーは 6 時間後から AE の発生頻度が急激に増大した．図 16 に示したように，すべての条件で AE 累積数の増加とともに荷重保持率は低下する傾向を示すが，乾燥条件より湿潤条件のほうが急激に低下した．また，湿潤条件において同じ AE 累積数では無処理ワイヤーは 403 ワイヤーより荷重保持率が低かった．カップリング処理の効果は湿潤条件下でより顕著に現れることが示された．定たわみ曲げ試験において，6 時間での縦弾性係数，2 mm 荷重値，2 mm 変形エネルギーは無処理ワイヤーより 403 ワイヤーが有意に高い値を示した（$p<0.05$）が，次第に差が小さくなった．永久変形量は 6 時間を過ぎた辺りから無処理ワイヤーと 403 ワイヤーの差が大きくなっている．これは浸漬後 6 時間後まではカップリング処理によって界面の剥離が抑制されているが，次第に界面接着効果が低下し，徐々に剥離したためと推測できる．

以上のことより，FRP ワイヤーは浸漬後 3～6 時間程度で吸水が完了し，樹脂の膨潤，可塑化が起こり，続いてガラス繊維／マトリックス間の界面接着効果の低下が進み，永久変形や荷重の低下を引き起こすが，逆にマトリックス内でガラス繊維が滑りやすくなることで明確な破断を起こしにくくなる．また，ガラス繊維にカップリング処理を施し，界面剥離の発生を抑制すれば，荷重保持率が高く維持される．このことは，耐水性の高いカップリング処理剤により，さらに耐久性の優れた FRP ワ

イヤーが開発できる可能性を示唆するものである.

結　論

口腔内環境下でのFRPワイヤーの吸水動態と，その機械的特性の経時的変化に及ぼす影響を調べるために，乾燥および湿潤条件における3点曲げ試験，応力緩和試験とAE計測を行い，さらに定たわみ曲げ負荷後の曲げ特性の経時的変化を観察し，以下の結論を得た.

1. 吸水が完了する時間は，応力緩和試験でのAEの増加，荷重保持率の低下が著しくなる時期3〜6時間とほぼ一致した.

2. 多数の試験片について同一条件下の試験を可能とする定たわみ曲げ試験を行った結果，負荷時間とともに永久変形量の増加，縦弾性係数，2 mm荷重値が低下し，これらは2 mm変形エネルギーにより単一の指標で総合的に評価できた.

3. 湿潤条件下での機械的特性低化の要因は吸水であり，マトリックスの吸水，可塑化が生じ，変形に伴うガラス繊維／マトリックス間の界面剥離，ガラス繊維の滑り，荷重および縦弾性係数の低下，永久変形量の増加を引き起こす.

4. カップリング処理は界面剥離を抑制し，機械的特性低下の抑制に効果があった.

5. 口腔内に類似した環境下でFRPワイヤーの経時的挙動を各種試験を導入して調べ，マトリックスとカップリング剤の吸水に対する対策等，臨床応用の実現に必要な改善点を明らかにした.

付　記

本論文の一部は第38回日本歯科理工学会学術講演会（平成13年10月，福岡），第39回日本歯科理工学会学術講演会（平成14年4月，東京），第41回日本歯科理工学会学術講演会（平成15年4月，東京）において発表した.

また，本研究は平成15年度科学研究費補助金基盤研究(B)(1)(14370685号）の補助により行った.

謝　辞

本稿を終えるにあたり，終始ご指導，ご校閲を賜りました北海道大学大学院歯学研究科口腔機能学講座歯科矯正学分野 山方秀一助手に甚大なる謝意を表します.本研究の遂行にあたり，快くご協力をくださいました，同講座豊泉　裕助手，同講座研究生宇賀　大氏，諏訪伸輔氏に深謝いたします．また，本研究にひとかたならぬご理解，ご協力くださいました同口腔健康科学講座物性歯科理工学分野 宇尾基弘助教授をはじめ，大川昭治助手，赤坂　司助手，菅原　敏技官に心より感謝いたします．さらに，本研究に種々ご協力いただきました同口腔機能学講座歯科矯正学分野および千葉工業大学工業化学科の教室員各位に厚く御礼申し上げます.

文　献

1) Newman GV. Epoxy adhesives for orthodontic attachments. Progress Rep Am J Orthod 1965；51：901－912.
2) Swartz ML. Ceramic brackets. J Clin Orthod 1988；22：82－89.
3) 加藤博重，福原達郎．新しい結紮方法— Quick Ligature Placer と O－Ring—．歯科評論 1983；494：10－13.
4) 加藤博重，小林廣之，清水畑明，大島久美子，北野誠弓，柴崎好伸ほか．結紮用エラスティック・リングの理工学的特性について．歯材器 1987；6：183－189.
5) 加藤博重．弾性高分子材料からなる矯正材料を用いた簡便な治療体系の確立．歯医学誌 1988；7：27－35.
6) Louis JT, Terrence MS, Steven OH, Lewis L. Force decay and deformation of orthodontic elastic ligatures. Am J Orthod Dentofac Orthop 1997；111：1－11.
7) Talass MF. Optiflex arch treatment of a skeletal Class Ⅲ openbite. J Clin Orthod 1992；26：245－252.
8) 森下　格，名方俊介，渡辺美枝子，中島昭彦．Q.C.Mの概念と材料．矯臨ジャーナル 1994；10：51－59.
9) Goldberg AJ, Burston CJ, Madjinikolaon I, Jancar J. Screening of matrices and fibers for reinforced thermoplastic intended for dental application. J Biomed Mater Res 1994；28：167－173.
10) Kennedy Ⅱ KC, Kusy RP. UV-cured pultrusion processing of glass-reinforced polymer composite. J Vinyl & Additive Tech 1995；1：182－186.
11) Kusy RP. Review of contemporary arch wires. Angle Orthod 1997；67：197－208.
12) Zufall SW, Kusy RP. Stress relaxation and recovery behavior of composite orthodontic archwire in bending. Europ J Orthod 2000；22：1－12.
13) 小林雅博，田賀井秀夫，黒木良克，丹波滋郎，尾野幹也．人工骨用ガラス繊維複合材の試作と性質．Orthop Ceram Implant 1984；4：79－82.
14) 瀬山雅博，黒木良克，新井治男，森下益太郎，川内邦雄ほか．人工骨用ガラス（C.P.S.A系ガラス）の細胞毒性試験．中部整災誌 1987；9：474－476.
15) 瀬山雅博，黒木良克，森下益太郎，小林雅博，田賀井秀夫．人工骨用ガラス（C.P.S.A系ガラス）の細胞毒性試験—第二報　骨由来細胞を用いて—．中部整災誌 1987；30：474－476.
16) 山方秀一，今井　徹，亘理文夫．繊維強化プラスチック型審美性矯正用ワイヤーの開発に関する基礎研究．北歯誌 1995；16：225－243.
17) Watari F, Kobayashi M, Yamagata S, Nagayama K, Imai T et al. Properties of the unidimensionally glass fiber reinforced composite wire for an esthetic orthodontic wire. Bioceramics (Proc.9th Int. Symp. On Ceramics in Medicin) 1996；469－472.
18) Watari F, Kobayashi M, Yamagata S, Nagayama K, Imai T et al. Structure and properties of the FRP esthetic orthodontic wire. Proc Int Conf on Microstructures and Functions of Materials (ICMF 96) 1996；141－144.
19) 相馬邦道，黒田勝也，堀部邦孝，飯田順一郎，野田孝夫，亘理文夫ほか．歯科用異種特性複合材料の開発．歯医学誌 1997；16：46－60.
20) Watari F, Yamagata S, Imai T, Kobayashi M, Nakamura S. The fabrication and properties of aesthetic FRP wires for use in orthodontics. J Mater Sci 1998；33：5661－5664.
21) Imai T, Watari F, Yamagata S, Kobayashi M, Nagayama K et al. Mechanical properties and aesthetic of FRP orthodontic wire fabricated by hot drawing. Biomaterials 1998；19：2195－2200.

22) 永山和典，亘理文夫，今井　微，山方秀一，小林雅博．審美性矯正用ワイヤーの水中浸漬による影響とコーティング処理に関する研究．北歯誌 1998；19：197－213.
23) 豊泉　裕，亘理文夫，今井　微，山方秀一，小林雅博．光重合法による曲げおよびねじり剛性を有する審美性矯正用ワイヤーの試作．歯材器 1999；18：429－440.
24) Imai T, Watari F, Yamagata S, Kobayashi M, Nagayama K, Nakamura S. Effects of water immersion on mechanical properties of new esthetic orthodontic wire. Am J Orthod Dent Orthop 1999；116：533－538.
25) 小林雅博，今井　微，山方秀一，永山和典，中村進治，亘理文夫，大川昭治．審美性歯科矯正ワイヤーの in vitro 試験．歯材器 1996；15（特 28）：54－55.
26) Imai T, Yamagata S, Watari F, Kobayashi M, Nagayama K, Toyoizumi H. Temperature-dependence of the mechanical properties of FRP orthodontic wire. Dent Mter J 1999；18：167－175.
27) 永山和典，山方秀一，山本隆昭，今井　微，中村進治，近藤清一郎，大川昭治，宇尾基弘，菅原　敏，亘理文夫．審美性矯正用ワイヤーの曲げ特性に及ぼす水中浸漬の影響．歯材器 1997；16（特 29）：163.
28) 尾上守夫，山口楠雄，仲佐博裕，佐野謙一，磯野英二，渡辺哲夫．AE の計測．尾上守夫．アコースティック・エミッションの基礎と応用．1：コロナ社；1976. p.30－55.
29) 須藤　一．材料試験法．2：内田老鶴圃新社；1980. p.59－63.

X-ray Absorption Fine Structure Studies on the Local Structures of Ni Impurities in a Carbon Nanotube

Kiyotaka Asakura,[†] Wang-Jae Chun,[†,††] Kazuyuki Tohji,[†††] Yoshinori Sato,[†††] and Fumio Watari[††††]
[†]*Catalysis Research Center, Hokkaido University, Sapporo, Hokkaido 001-0021*
[††]*Core Research for Evolutional Science and Technology, Japan Science and Technology Corporation, Sapporo, Hokkaido 001-0021*
[†††]*Graduate School of Environmental Studies, Tohoku University, Aoba, Sendai, 980-8579*
[††††]*Graduate School of Dental Medicine, Department of Biomedical, Dental Materials & Engineering, Hokkaido University, Kita 13 Nishi 7 Sapporo, Hokkaido 060-8586*

(Received October 21, 2004; CL-041243)

Local structure around Ni impurities in a carbon nanotube was studied by X-ray absorption fine structure (XAFS). The Ni was present in the form of Ni particles before the purification process. After the purification Ni content was decreased to a few hundreds ppm. The Ni K-edge XAFS could be measured by a 19 element solid-state detector. The Ni species was strongly bound to the carbon of the carbon nanotube with a Ni–C covalent bonds at 0.173 nm.

Carbon nanotubes draw much attention as new materials, which have wide applications to many fields such as electric devices, hydrogen storage materials, field emission display, AFM tip, and so on.[1] Since carbon nanotubes are composed of only carbon atoms and are expected to have biocompatibility, the researches for the biological application have been started such as a drag delivery system, scaffolds for cell engineering, artificial bones, dental roots, and cell culture media.[2] Chemical vapor deposition (CVD) synthesis method using catalysts such as Ni, Fe, Fe–Ni, and Ni–Mo is one of promising methods for large-scale production of carbon nanotubes.[3] Ni is one of the best catalysts to produce carbon nanotubes but it often shows toxic properties to a living body. Although most of Ni in the carbon nanotube can be removed by the HCl treatment, it is important to know the metabolism, chemical state, and structure of Ni impurity left in the carbon nanotubes after the HCl treatment in order to apply the nanotubes to medical and biological fields safely. In this paper, we report the characterization of the chemical state of residual Ni species before and after the purification processes of a carbon nanotube by XAFS (X-ray absorption fine structure) technique. Because the amount of Ni species after the purification is about a few hundred ppm, it is difficult to estimate the Ni chemical state by conventional techniques. We carried out fluorescence XAFS analysis of Ni impurity in the carbon nanotube. We found that the Ni species was strongly fixed to the carbon of a carbon nanotube through a Ni–C covalent bond.

Carbon nanotube was synthesized by a CVD method using Ni catalyst. It was purified by a calcination followed by 6 M HCl treatment for 6 h in order to remove the carbon nanoparticles and Ni catalysts.

XAFS measurements were carried out at BL9A of the Photon Factory in Institute for Structure Material Science (KEK-PF) using a Si(111) double crystal monochromator.[4] (99G280, 2001G287) The incident and transmitted X-rays were monitored by ionization chambers filled with nitrogen. The fluorescence X-ray was detected by a 19 element SSD (solid state detector) (Camberra Co.) The dead times of SSD were corrected according to the literature.[5] The XAFS analyses were carried out by REX2000 (Rigaku Co) using phase shift and amplitude functions derived from FEFF8.[6,7]

Figure 1 showed the Fourier transforms of Ni K-edge XAFS oscillations before the purification over $k = 30$–$150\,\mathrm{nm}^{-1}$. We measured the XAFS oscillation in a transmission mode because we had an enough edge jump. We found several peaks. The first and main peak appeared at 0.25 nm, which corresponded to that of the Ni–Ni distance in the first shell of Ni metal. The longer Ni–Ni peaks clearly appeared, which were corresponding to the 2nd, 3rd and 4th shells in the Ni fcc structure. The curve fitting analysis showed that the coordination number and bond distance of the first shell Ni–Ni bond were 12 and 0.248 nm, respectively, indicating that the Ni was present in a metal particle larger than 5 nm judging from the coordination numbers of the first and the higher shells which were almost equal to that of the bulk Ni species.[8]

When the Ni metal particles were removed by the HCl treatment, we could not observe Ni K-edge in a transmission mode any more. Thus we used a fluorescence mode to obtain Ni XAFS oscillations. According to the Ni Kα fluorescence peak intensity, the amount of Ni can be estimated to be about a few hundred ppm. Figure 2 shows the X-ray near edge structure of Ni species in the carbon nanotube before and after the HCl treatment to-

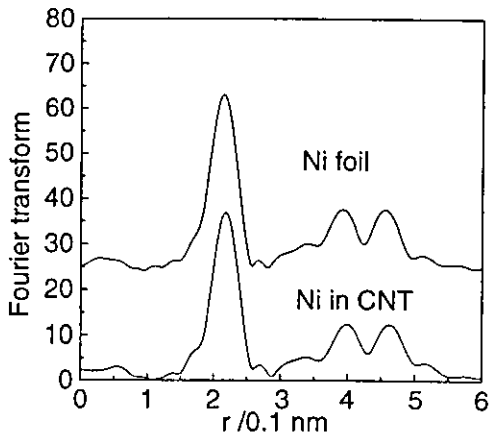

Figure 1. Fourier transforms of XAFS oscillations for Ni catalysts in the carbon nanotube and Ni foils.

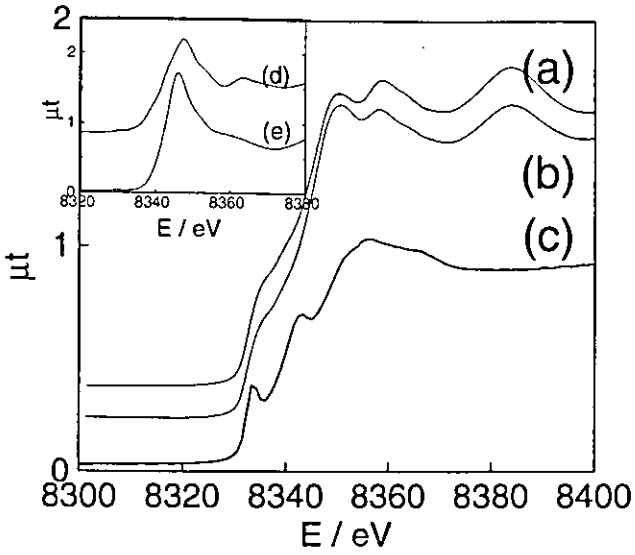

Figure 2. Ni K-edge XANES of (a) Ni foil, (b) Ni species in the carbon nanotube before purification, and (c) that after the purification. (d) and (e) in the inset showed XANES spectra for NiO and $Ni(NO_3)_2 \cdot 9H_2O$.

gether with reference compounds. The XANES (X-ray absorption near edge structure) spectrum after the HCl treatment was completely different from that before the HCl treatment and Ni foil, indicating that the metallic Ni particles were completely removed by the HCl treatment. The XANES spectrum of the sample after the HCl treatment was different from those of NiO and $Ni(NO_3)_3 \cdot 9H_2O$. The residual Ni species was not simple oxide or aquo complex ions. Peaks in the XANES spectrum appeared at the similar positions as in the spectrum of the deactivated Ni catalyst after the CH_4 decomposition reaction though the peak heights were much stronger in the present spectrum.[9]

Figure 3 shows the Fourier transforms of Ni K-edge XAFS of Ni species in the carbon nanotube after the HCl treatment. Peaks appear at 0.16 and 0.22 nm. We carried out curve fitting analysis for the first shell assuming Ni–C bond. The bond distance and coordination number were 0.177 nm and 1.5, respectively. The second shell peak could be assigned to Ni–Ni at 0.247 nm with its coordination number 0.8. Ni–C distance 0.177 nm was smaller than 0.186 and 0.184 nm found in Ni_3C and $Ni(CO)_4$, respectively. Thus the Ni species was fixed strongly to carbon nanotube through a covalent bond. Since carbon nanotubes were stable in the living body, Ni impurity may stay there for a long time and may bioaccumulate. We recommend that the Ni catalyst should not be used to the production of the carbon tube if it is used as a biomaterial.

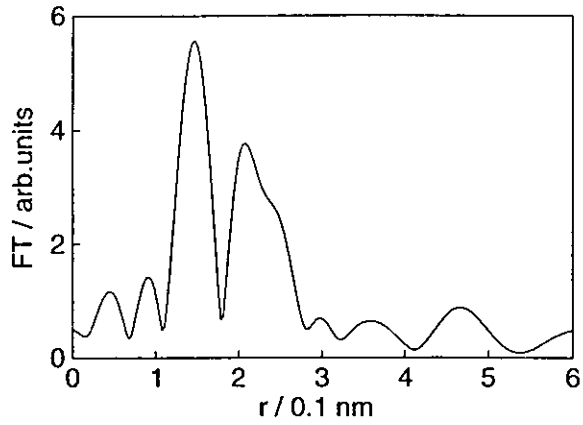

Figure 3. Fourier transform of Ni K-edge EXAFS for the Ni species in the carbon nanotube after the HCl treatment.

References

1 P. J. F. Harris, "Carbon Nanotubes and Related Structures: New Materials for the Twenty-first Century," Cambridge University Press, Cambridge (1999).
2 "Nanotoxicology and Development of Carbon Nanotubes and Nano/Micro Particles for Biomedical Applications," ed. by F. Watari, Springer Verlag, Berling, to be published.
3 M. Endo, Y. A. Kim, T. Hayashi, T. Yanagisawa, H. Muramatsu, M. Ezaka, H. Terrones, M. Terrones, and M. S. Dresselhaus, *Carbon*, **41**, 1941 (2003).
4 M. Nomura, *KEK Report*, **98-194**, 1 (1998).
5 M. Nomura,*KEK Report*, **98-4**, 1 (1998).
6 K. Asakura, "X-ray Absorption Fine Structure for Catalysts and Surfaces," ed. by Y. Iwasawa, World Scientific, Singapore (1996), pp 33–58.
7 S. I. Zabinsky, J. J. Rehr, A. Ankudinov, R. C. Albers, and M. J. Eller, *Phys. Rev. B*, **52**, 2995 (1995).
8 R. B. Greegor and F. W. Lytle, *J. Catal.*, **63**, 476 (1980).
9 S. Takenaka, H. Ogihara, and K. Otsuka, *J. Catal.*, **208**, 54 (2002).

Published on the web (Advance View) February 12, 2005; DOI 10.1246/cl.2005.382

A Possibility of XANAM (X-ray Aided Non-contact Atomic Force Microscopy)

Shushi Suzuki, Yuichiro Koike, Keisuke Fujikawa, Wang-Jae Chun, Masaharu Nomura,† and Kiyotaka Asakura*
Catalysis Research Center, Hokkaido University, Kita-ku 21-10, Sapporo, 001-0021
†*Photon Factory, Institute of Material Structure Science, High-Energy Accelerator Organization, Oho 1-1, Tsukuba 305-0801*

(Received January 26, 2004; CL-040095)

We have measured a frequency shift of the noncontact atomic force microsocpy (NC-AFM) cantilever above Au islands when we scanned the X-ray energy around the Au L_3 absorption edge. We have found a clear peak of the frequency shift just above the Au L_3 absorption edge. This novel phenomenon suggested that the combination of energy-variable X-rays and NC-AFM provides us a new way of nano level chemical mapping of surfaces.

A surface chemical mapping on an atomic level is very important in nanoscience to understand the chemical processes occurring at the surfaces of catalysts, sensors, and electronic devices. Since the invention of the scanning tunneling microscopy (STM)[1] in 1982, atomic-level spatial resolution of conductive material surfaces has been achieved and the invention of the noncontact atomic force microscopy (NC-AFM)[2] in 1995 has made it possible to measure insulator surfaces. However, it is still difficult to distinguish chemical species directly by these STM and NC-AFM. Many efforts have been done to obtain chemical information by developing techniques of scanning probe microscopy (SPM) family such as STM inelastic tunneling spectroscopy,[3] STM light emission spectroscopy,[4,5] infrared scanning near-field optical microscopy,[6] X-ray excited STM.[7] In this brief communication, we report a novel phenomenon that will be a base for a new elemental analysis at the atomic level by SPM, named "X-ray Aided Noncontact Atomic force Microscopy (XANAM)."

The NC-AFM has a wide applicability to insulator inorganic oxides and organic polymers.[8] Atomic level observations of insulating oxide surfaces have recently been reported.[9–13] NC-AFM imaging is attained by detecting the frequency shift of the cantilever, which can simply be explained by the value proportional to the attractive force gradient between a tip of the cantilever and the surface atoms.[14] Theoretical and computational analyses show that the forces are not only physical forces such as van der Waals force and electrostatic force but also chemical bonding force such as a covalent bonding. The chemical bonding force may depend on the electron density of bonding and antibonding orbitals. If the electron density of these orbitals can be controlled, one may control the interaction between the surface atom and the cantilever. X-ray is one way to alter the electron density of bonding or antibonding orbitals by exciting core electron. The core electron has a binding energy specific to elements and their chemical state. Thus one can get a chemical mapping using the NC-AFM aided by X-ray irradiation. To test the above hypothesis, we carried out a simple experiment to see how the frequency shift depends on X-ray energies near the absorption edge. We found a sudden frequency shift of the NC-AFM cantilever just above the Au L_3 X-ray absorption edge described later.

The experiments were performed at BL7C of the Photon Factory, Institute of Material Structure Science, High Energy Accelerator Organization (KEK-IMS-PF). A noncontact atomic force microscope was operated under ultrahigh vacuum (UHV) conditions with a piezoresistive AFM cantilever (NIKON). The tip apex of the cantilever was composed of silicon nitride. A typical resonance frequency and force constant of the cantilever were 88 kHz and 150 Nm^{-1}, respectively. The partially Au-covered sample was prepared by vacuum evaporation of Au on a Si substrate through a 1000 L Ni mesh put on the substrate. The sample was set on the microscope stage with its surface standing vertically. Two X-ray entrance and exit beryllium windows were placed at the front and backside of the UHV chamber. The microscope stage had three kinds of freedom to set the sample surface on the X-ray pass: x- and y- horizontal movements and a rotation around vertical (z) axis. We focused an X-ray beam on the sample position by a sagital focusing Si(111) double-crystal monochromator.[15] Because of the beam time limitation, we could not optimize the NC-AFM imaging conditions. The spatial resolution of the microscope was a few nanometer, which was confirmed by the observation of a PZT layer sample surface composed of fine particles with diameter from 10 to 20 nm, as shown in Figure 1.

The NC-AFM observation of the partially Au-covered Si sample was carried out in a constant frequency shift mode with constant excitation amplitude of the cantilever with X-ray irradiation at 11850 eV. Figure 2 shows a typical NC-AFM image of a sample surface observed at room temperature. Au-deposited region and Si region were clearly distinguished by their height difference. The Si region was probably covered with native Si oxide layer because no treatment to remove oxide layer was done in the UHV chamber. The constant frequency shift of the cantilever was −20 Hz during the observation. Then we put the cantilever above the Au island, as shown in Figure 2 by a square, and stopped the scan feedback routine of the cantilever. We started to measure frequency shift dependency on the X-ray energy around

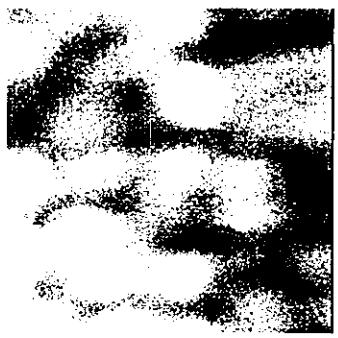

Figure 1. A NC-AFM image of PZT layer sample under X-ray irradiation, $70 \times 70\,nm^2$, $\Delta f = -20$ Hz, $A_0 = 27$ nm.

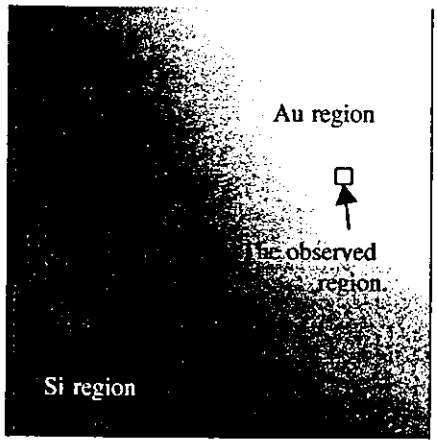

Figure 2. NC-AFM image of partial Au-deposited Si surface, $3.5 \times 3.5\,\mu m^2$, $\Delta f = -20\,Hz$, $A_0 = 27\,nm$.

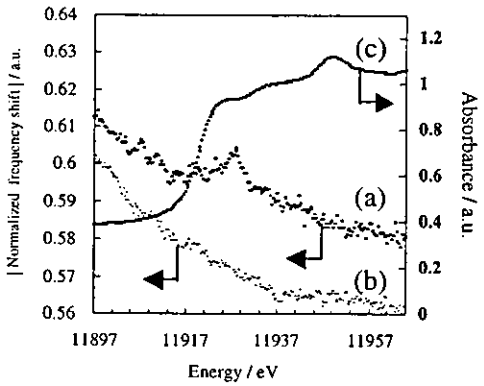

Figure 3. Frequency shift spectra normalized by I_0 on both Au (a) and Si (b) regions together with absorption spectrum of Au foil (c).

the Au L_3 absorption edge. For comparison we carried out the same experiment on the bare Si surface in the same energy range.

Figure 3 shows the frequency shift spectra above both Au and Si regions together with an absorption spectrum of Au foil. The frequency shift signal was integrated by a F–V converter circuit with duel time of 2 s, and was normalized by incident X-ray intensity which was simultaneously recorded by the ionization chamber in front of the NC-AFM chamber. We plotted the absolute value of the normalized frequency shift. Generally, the frequency shift is negative in the attractive force region. Increasing the absolute value of the shift corresponded to the enhancement of attractive force between the cantilever and the sample surface. Each spectrum was recorded with increasing the X-ray energy.

When the X-ray was irradiated, the sample was heated by the X-ray and changed its position gradually related to the tip apex by the thermal drift. Consequently the monotonous variations in the background were found. In addition to these background variations, we found a distinctive peak around the X-ray energy of 11925 eV in the Au region, while no peak was found in the Si region within the same energy range. We observed repeatedly the peak at the same X-ray energy at different Au regions but no peak was found at Si regions. The presence of the peak clearly demonstrates that the X-rays around the absorption edge energy affect the frequency shift of the NC-AFM cantilever. Generally, the frequency shift is negative in the attractive force region. Thus, increasing the absolute value of the shift corresponded to the enhancement of attractive force between the cantilever and the sample surface. Note that the normalized frequency shift did not follow the absorption spectrum of Au foil, namely, the spectral feature of Au region did not have an absorption edge but a peak. It means the phenomenon is not simply related to the photoabsorption process.

The following origins to enhance the attractive force between the cantilever and the sample surfaces can be proposed.

(1) Excitation of photoelectron to a bonding orbital to strengthen the covalent bond, as mentioned above.
(2) Local electric field enhancement around cantilever apex like Surface Enhanced Raman Spectroscopy (SERS).

We are planning to measure element-selected NC-AFM image by this system soon. Although the detailed mechanism and physics are unclear at the moment, the phenomenon suggested that NC-AFM could distinguish Au from Si under the X-ray irradiation tuned at the absorption edge energy. This phenomenon will lead to a new nano-level element-selected imaging method aided by X-ray called as XANAM.

This work was supported by the New Energy and Industrial Technology Development Organization (NEDO) and the Japan Science and Technology Corporation (JST). The experiments were carried out under the approval of Photon Factory Advisory Committee (PAC: Proposal No. 2003G301).

References

1 G. Binnig and H. Rohrer, *Helv. Phys. Acta*, **55**, 726 (1982).
2 F. J. Giessibl, *Science*, **267**, 68 (1995).
3 B. C. Stipe, M. A. Rezaei, and W. Ho, *Science*, **280**, 1732 (1998).
4 K. Ito, S. Ohyama, Y. Uehara, and S. Ushioda, *Surf. Sci.*, **324**, 282 (1995).
5 Y. Kim, T. Komeda, and M. Kawai, *Phys. Rev. Lett.*, **89**, 126104 (2002).
6 D. T. Schaafsma, R. Mossadegh, J. S. Sanghera, I. D. Aggarwal, J. M. Gilligan, N. H. Tolk, M. Luce, R. Generosi, P. Perfetti, A. Cricenti, and G. Margaritondo, *Ultramicroscopy*, **77**, 77 (1999).
7 K. Tsuji and K. Hirokawa, *Jpn. J. Appl. Phys.*, **34**, L1506 (1995).
8 R. García and R. Pérez, *Surf. Sci. Rep.*, **47**, 197 (2002).
9 K. Fukui, H. Onishi, and Y. Iwasawa, *Phys. Rev. Lett.*, **79**, 4202 (1997).
10 H. Hosoi, K. Sueoka, K. Hayakawa, and K. Mukasa, *Appl. Surf. Sci.*, **157**, 218 (2000).
11 T. Kubo and H. Nozoye, *Phys. Rev. Lett.*, **86**, 1801 (2001).
12 K. Fukui, Y. Namai, and Y. Iwasawa, *Appl. Surf. Sci.*, **188**, 252 (2002).
13 S. Suzuki, Y. Ohminami, T. Tsutsumi, M. M. Shoaib, M. Ichikawa, and K. Asakura, *Chem. Lett.*, **32**, 1098 (2003).
14 S. Morita, R. Wiesendanger, and E. Meyer, "Non-contact Atomic Force Microscopy," Springer, Berlin (2002).
15 M. Nomura, A. Koyama, and Sakurai, "KEK Report," (1991), Vol. 91-1, p 1.

Published on the web (Advance View) April 24, 2004; DOI 10.1246/cl.2004.636

Japanese Journal of Applied Physics
Vol. 43, No. 11A, 2004, pp. 7682–7688

Observation of Element-Specific Energy-Filtered X-Ray Photoemission Electron Microscopy Images of Au on Ta Using a Wien Filter Type Energy Analyzer

Hideyuki YASUFUKU[1,2], Yusuke OHMINAMI[1], Tetsuya TSUTSUMI[1], Hironobu NIIMI[1], Nobuaki MATSUDAIRA[1], Kiyotaka ASAKURA[1], Makoto KATO[3], Yuji SAKAI[3], Yoshinori KITAJIMA[4] and Yasuhiro IWASAWA[5]

[1]*Catalysis Research Center, Hokkaido University, Kita 21-10, Kita-ku, Sapporo 001-0021, Japan*
[2]*NIMS, SPring-8, 1-1-1 Kouto, Mikazuki-cho, Sayo-gun, Hyogo 679-5198, Japan*
[3]*JEOL Ltd, 3-1-2 Musashino, Akishima, Tokyo 196-8558, Japan*
[4]*Photon Factory, Institute of Material Structure Science, Oho 1-1, Tsukuba 001-0021, Japan*
[5]*Department of Chemistry, Graduate School of Science, The University of Tokyo, Hongo, Bunkyo-ku, Tokyo 113-0033, Japan*

(Received August 11, 2003; revised March 24, 2004; accepted July 30, 2004; published November 10, 2004)

We have shown the possibility of a Wien filter as an energy analyzer for the energy-filtered X-ray photoemission electron microscopy (EXPEEM) by obtaining images of Au islands on a Ta substrate using an inner shell photoelectron excited by an X-ray with a photon energy of 2300 eV. When the photoelectron with kinetic energy of nearly 0 eV was selected, brighter Au islands were observed. When the kinetic energies of photoelectrons passing the Wien filter are set at those of Au $3d_{5/2}$ and Ta $3p_{3/2}$ photoelectrons, the Au and Ta regions appeared brighter, respectively, indicating that the chemical imaging was successful using a high energy X-ray and a Wien filter energy analyzer. [DOI: 10.1143/JJAP.43.7682]

KEYWORDS: energy-filtered X-ray photoemission electron microscopy, PEEM, XPEEM, EXPEEM, Wien filter, Au, Ta, Surface imaging, spectromicroscopy, XPS

1. Introduction

A photoemission electron microscopy (PEEM) can provide a promising approach to the real-time investigation of nanoscale (approximately 10 nm order) surface chemical processes such as diffusion, adsorption, desorption and reaction. Rotermund and coworkers observed unique spatio-temporal concentration patterns of adsorbates during the CO oxidation reaction on Pt(100) and Pt(110) surfaces by PEEM, which have offered new information about the surface nonlinear processes.[1,2] They used a Deuterium lamp (with a photon energy of about 6 eV) to excite the photoelectrons and thus the PEEM is sensitive to the surface work functions. One can identify the surface chemical species directly only in a simple system where the work functions of chemical species are well known and are significantly different from each other. Application of X-rays, which can excite inner shell electrons, will provide us with chemical information such as the kind of elements and their chemical state by analyzing the absorption edge energy or the kinetic energy of emitted photoelectrons as summarized in Table I. In the category I, the element analysis is achieved with a tunable X-ray source such as synchrotron radiation, and spatial resolution is attained by a conventional PEEM method.[3–5] This gives an image with good contrast as mentioned below, but the use of synchrotron radiation is essential. Category II is a combination method of PEEM and well-known X-ray photoelectron spectroscopy (XPS) methods.[6] This is called EXPEEM (energy-filtered X-ray PEEM) in this paper. The EXPEEM has the merit of being able to realize chemical imaging of the surface using an X-ray source with a fixed energy such as bremsstrahlung radiation. However, until now, the EXPEEM has been realized with an undulator of the 3rd generation synchrotron radiation as a light source.[7–11] The kinetic energies of photoelectrons are often analyzed using a conventional hemispherical energy analyzer. The problem of using the conventional energy analyzer is that it has a nonlinear electron optical axis, which hinders easy operation of the system. Thus an energy analyzer in a collinear arrangement is preferable. Recently energy analyzers retaining a linear electron optical axis have been developed, such as a time-of-flight analyzer and a retarding field energy analyzer.[12–14]

We use a Wien filter type energy analyzer which has a linear electron optics and can remove higher order aberrations in an energy filter.[15,18,35] In the Wien filter, the electric field ($\boldsymbol{E}$) and magnetic field ($\boldsymbol{B}$) are applied perpendicularly as shown in Fig. 1(a). Consequently, the forces from the electrostatic and magnetic fields are applied oppositely. The Lorenz force ($e\boldsymbol{v} \times \boldsymbol{B}$) from the magnetic field has an amplitude proportional to the velocity ($\boldsymbol{v}$) of the electron. When these forces are balanced, i.e., $\boldsymbol{E} = \boldsymbol{v} \times \boldsymbol{B}$, an electron passes through the Wien filter without changing direction.[16,17] This condition is called the Wien condition. When a slit is placed after the Wien filter, one can select electrons which satisfy the Wien condition. To observe an energy-filtered image, the Wien filter should have a lens function in addition to an energy analyzer function. This is accomplished by the superposition of the quadrupole electrostatic fields. Finally, the projection lenses are adjusted to give an energy-filtered image on a screen as shown in Fig. 1(b).

Compared with the standard hemispherical energy analyzer, the advantages of using the Wien filter as an energy analyzer are as follows:[15,16,18,35]

Table I. Summary of element-specific XPEEM system.

Category	Spatial resolution	Element specificity	Photon Energy	Detector	Energy Analyzer	References
I	electron optics	absorption edge	tunable	spatial resolution	none	3–5
II	electronic optics	kinetic energy	fixed	spatial resolution	imaging type	8,10,11

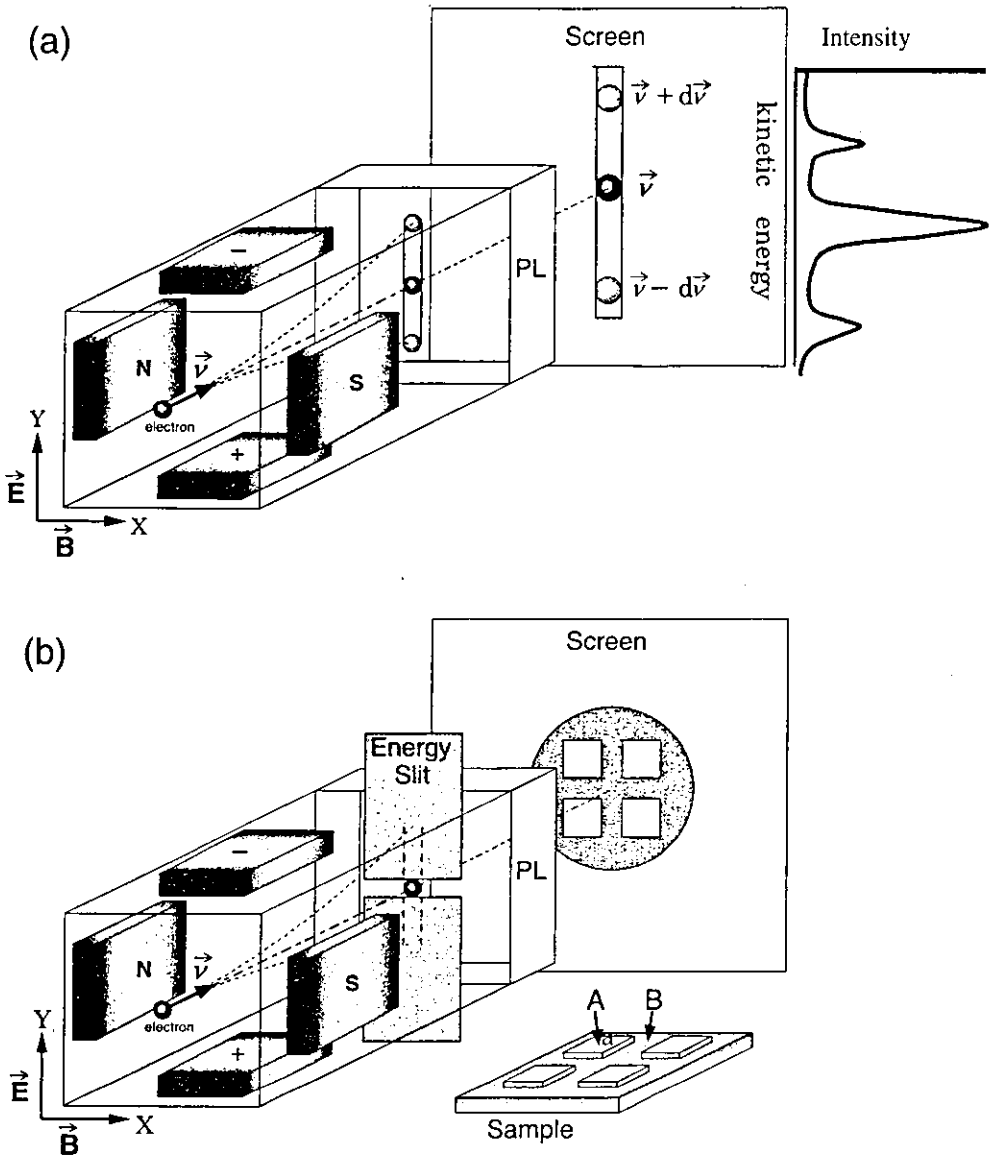

Fig. 1. Schematic view of the principle of the Wien filter. (a) Dispersion mode: Electrons coming from the left with velocity v travel in a straight line when $F = e(E - v \times B) = 0$ is satisfied. Otherwise the electrons are bent up or down according to their velocity. (b) Imaging mode: Observing an energy-selected image with a selected kinetic energy. In this case, island A is composed of element a. When a photoelectron characteristic of element a is selected, island A appeared bright in the image.

(1) A collinear arrangement of the electron optics simplifies the optimization processes of the optical axis and imaging conditions. The electron can pass through the filter when no electric and magnetic fields are applied. Thus it is possible to increase the fields of the Wien filter by monitoring the electron beam at the screen continuously, which makes it much easier to adjust the energy filtering conditions.
(2) Corrections for the second and the third order aberrations in the energy analyzer are possible by adjusting the Fourier components of the electric and magnetic fields, though the correction of the second order aberrations in the hemispherical type energy analyzer is difficult.

The Wien filter has been used in the metastable electron emission microscopy (MEEM).[15,25-28] The MEEM performs chemical imaging through the distribution of vacant and filled electron states near the Fermi level. Yamamoto *et al.* observed energy-filtered MEEM images of the Si/SiO_2 using the Wien filter. The accumulation time and the lateral resolution for the 7 eV kinetic energy electrons were 10 min and 0.2 μm, with the energy width 2 eV, respectively.[26] On the other hand, the core electrons with higher binding energies have much smaller cross sections and thus the emission probability of the X-ray photoelectron became smaller. Yamaguchi *et al.* attempted to obtain an energy-filtered image using a conventional Al K_α X-ray source, but could not obtain the element-selected image.[19,20] Therefore, we have brought the EXPEEM system to the Photon Factory, a 2.5 GeV synchrotron radiation facility, to explore the possibility of using the Wien filter as an energy analyzer for the EXPEEM. In our previous communication we showed the possibility of obtaining the EXPEEM image using the Wien filter energy analyzer.[28] In this paper we report the experimental conditions and the results of the Au island deposited on a Ta substrate in greater detail. We also

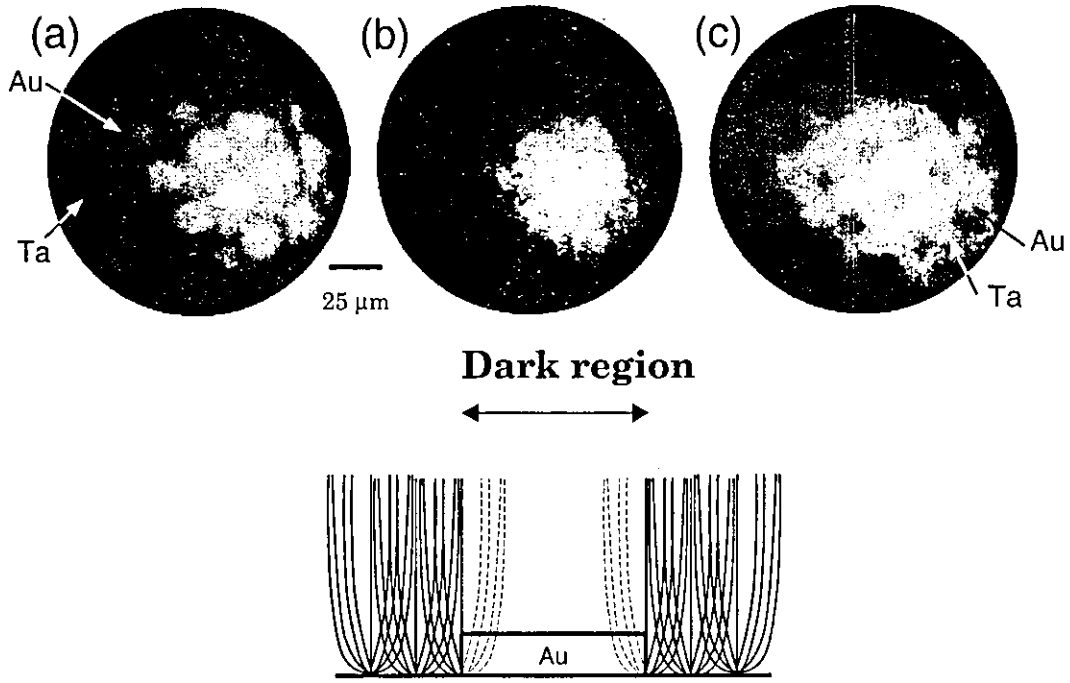

Fig. 2. Photon energy dependence of total electron yield XPEEM images. Size and separation of Au islands are 10 μm and 25 μm, respectively. Accumulation time was 2 min. Incident photon energies were 2300 eV (a), 2240 eV (b), and 2195 eV (c), while the absorption edge energies of Au and Ta are 2291 eV for Au M_4 ($3d_{3/2}$), 2206 eV for Au M_5 ($3d_{5/2}$), and 2194 eV for Ta M_3 ($3p_{3/2}$). (d) schematically explains the slit effect of the Au islands when the Ta $3p_{3/2}$ photoelectrons are used for imaging.

add new data for the EXPEEM image using an undulator beam line. Oxide-supported Au small particles have recently drawn much attention as a low-temperature oxidation catalyst.[22–24] The interface between Au and oxide is suggested to be the active site[22] and the EXPEEM may provide the chemical state at the interface region.

2. Experimental

2.1 Instrument

The EXPEEM system used in this work was originally developed as a low energy electron microcopy (LEEM)-MEEM system,[15,25–28] which was improved to obtain the EXPEEM system.[19–21] The instrument consists of a sample preparation chamber, and a measurement chamber equipped with an emission electron microscope as described elsewhere.[19,20] For the EXPEEM measurement, we used synchrotron radiation emitted from a bending magnet at BL11B of the Photon Factory (KEK-PF) operated at 2.5 GeV-300 mA. In order to excite the core-level electrons of the metal species, we chose the X-ray beam line with a variable photon energy between 2000–3900 eV. Although the excitation of the photoelectron by a high-energy X-ray has a disadvantage in terms of the EXPEEM imaging because of the high secondary electron background and the small photoemission cross section, one can obtain well-separated photoelectron peaks contrary to the VUV-excited EXPEEM image.[8–10] The beam was focused to 7 mm × 2 mm using a Ni-coated bent cylindrical mirror. The X-ray was monochromatized by a Ge (111) monochromator. The higher harmonics were rejected by a total reflection mirror after the double crystal monochromator. Photon flux was estimated to be 10^{11} photons/s at maximum. In order to reduce background electron emission due to the undesired irradiation of the sample holder or other parts of the instrument, an incident X-ray slit was narrowed and the sample was illuminated by a 1 mm × 1 mm beam. Thus the effective photon flux at the sample was approximately 10^{10} photons/s. The incidence angle of the X-ray beam was 70° with respect to the surface normal. We also used X-ray in the same energy range emitted from an undulator beam line (BL2A). The 5th order higher harmonics emitted from the undulator was monochromatized by another Ge(111) double crystal monochromator. The photon intensity at the sample was one order higher at BL2A than that at BL11B.

2.2 Sample preparation

We have prepared Au square islands on a Ta plate by the vacuum evaporation of Au. The base pressure of the evaporation chamber was 5×10^{-8} Torr. The Ta plate was covered with a Ni mesh. The thickness of the Au island was measured to be 1 μm by a laser morphology analyzer microscope (LT, Keyence Co.). The mesh had 10 μm square openings with a periodicity of 25 μm. The sample was then transferred to the UHV chamber and sputtered with an Ar^+ ion. By this treatment, the Ta oxide layer could not be removed, although the clean Au surface was recovered.[29]

3. Result and Discussion

3.1 Total electron imaging using an absorption edge

Figure 2(a) shows the total-electron yield XPEEM image of Au islands on a Ta sheet, to which the Wien filter was not applied. We did not use the angle-limiting aperture. Accumulation time for this image was 2 min. In Fig. 2(a) the photon energy was fixed at 2300 eV, just above the Au M_{IV} edge (E_B = 2291 eV, $3d_{3/2}$). Consequently, the bright region corresponds to the Au-deposited area and the dark region corresponds to the Ta area.

The number of emitted photoelectrons is decreased when

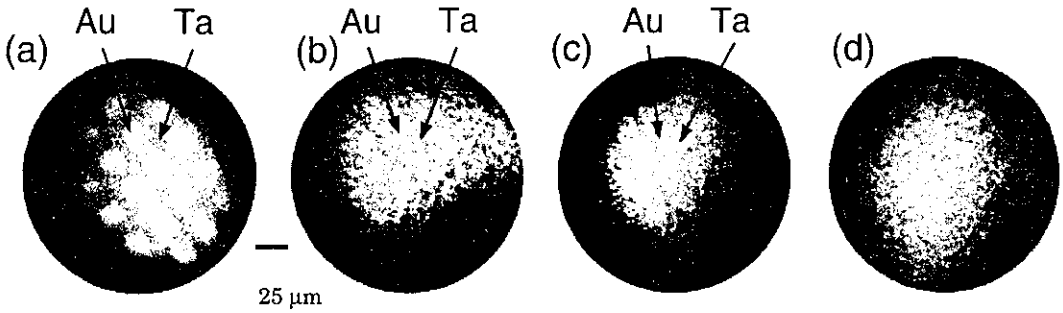

Fig. 3. Energy-filtered XPEEM images of Au on Ta substrate. Kinetic energies of the images are 0 eV (a), 60 eV (b), 102 eV (c), and 112 eV (d) and accumulation times were 30 s (a), 1 min (b), 10 min (c), and 10 min (d). Photon energy was 2300 eV. Photoelectron energy of (b) mostly corresponded to Au $3d_{5/2}$ while that of (c) corresponded to Ta $3p_{3/2}$.

the X-ray energy becomes lower than that of the absorption edge. Figures 2(a)–2(c) show the photon energy dependences of XPEEM images. The incident photon energy was varied from 2300 eV [Fig. 2(a)] which was just at the Au M_{IV} edge, to 2195 eV [Fig. 2(c)] which was just at the Ta M_{III} and at less than Au M_V edges. In Fig. 2(b), where the incident photon energy ($h\nu = 2240$ eV) was greater than the Au M_V ($E_B = 2206$ eV, $3d_{5/2}$) and Ta M_{III} ($E_B = 2194$ eV, $3p_{3/2}$) edges, the Au island was still slightly brighter than the Ta area. In Fig. 2(c), the contrast of the image was inverted. Bright regions corresponded to the Ta area and dark regions corresponded to the Au area, since the incident photon energy (2195 eV) was greater than the Ta M_{III} edge but less than the Au M_V edge. The apparent size of the Au island in Fig. 2(a) was approximately 15 μm, while the real size of the Au island was 10 μm. This was due to the poor spatial resolution of the system. Because we would like to have an image with sufficient intensity, we removed the angle limiting aperture and the spatial resolution became 2–3 μm. On the other hand, the size of Au in Fig. 2(c) was 10 μm which was the same as the real island size, even if the imaging conditions are the same in Figs. 2(a) and 2(c). Figure 2(a) did not give the Au island because of a type of artifact.[30–32] Since we did not use an angle limiting aperture, the EXPEEM system could accept many electrons from Au islands with large emission angles in the case of Figure 2(a), which increased the spherical aberrations. Because the spatial resolution in this case was mainly determined by the spherical aberrations of the objective lens, the Au islands appeared larger than their real size. On the other hand, in the case of Fig. 2(c), more electrons were coming from the Ta substrate than from the Au islands so that these electrons made images. Half of the electrons coming from the Ta region at or near the boundary of the Au islands were cut by the side walls of the Au islands as shown in Fig. 2(d). In other words, the Au islands played the role of the angle-limiting slit and this effectively decreased the spherical aberrations of the image in Fig. 2(c). This explanation was confirmed by the EXPEEM observation of Au islands at BL2A using an angle-limiting aperture, which is described later. In this case we could observe the 10 μm Au islands.

As Tonner *et al.* have pointed out, the monochromatized and continuously energy-varied X-ray can provide chemical contrast due to the local difference of the X-ray absorption edge energies by measuring the total electron yield.[33] In this case, a synchrotron radiation source is essential and an in-lab X-ray source cannot be applied. Moreover if one wants to measure carbon, nitrogen and oxygen which are important in chemical reactions, their binding energies appear at around 300–600 eV, a range which cannot be covered by a crystal monochromator; therefore, one has to change the beam line. From these viewpoints it is more desirable to develop the EXPEEM, which can give the chemical contrast by selecting the kinetic energy of photoelectrons.

3.2 EXPEEM imaging using a Wien filter

After obtaining the total electron image, we gradually applied the electric and magnetic fields to the Wien filter while observing the image. Figures 3(a)–3(d) showed the energy-selected images of XPEEM. The incident photon energy was fixed at 2300 eV. The pass energy of the Wien filter was 880 eV and the width of the selected electron energy was estimated to be 15 eV. First, the lens conditions were established for the photoelectrons with kinetic energy = 0 eV, as shown in Fig. 3(a). We changed the retarding voltage of the retardation lens to select the kinetic energy of photoelectrons passing through the energy selection slit. In order to determine the focus conditions, we adjusted only the potential of the second electrode in the cathode objective lens. The kinetic energies of the selected photoelectron in Figs. 3(a)–3(d) were 0 eV, 60 eV, 102 eV and 112 eV, respectively. The accumulation times for obtaining each image were 30 s, 1 min, 10 min, and 10 min, respectively. When photoelectrons with $E_{kin} = 0$ eV were selected [see Fig. 3(a)], the brighter regions corresponded to the Au-deposited areas and the darker regions corresponded to Ta areas, since the Au $3d_{3/2}$ photoelectrons were mainly used as a contrast formation. In Fig. 3(b), the kinetic energy of the photoelectron was set at 60 eV, which was higher than the kinetic energy of Au $3d_{5/2}$, Au-deposited areas were observed to be slightly brighter than Ta areas because the emission of inelastic photoelectrons, and secondary electrons arising from Au $3d_{5/2}$ photoemission were present in this energy region. Figure 3(c) showed the EXPEEM image at $E_{kin} = 102$ eV, which corresponded to the Ta $3p_{3/2}$ photoelectron peak. The contrast of this image was in reverse to those found in Figs. 3(a) and 3(b), with the bright and the dark regions corresponding to the Ta and Au areas, respectively. Figure 3(d) shows the energy-filtered image at $E_{kin} = 112$ eV, the kinetic energy of which was higher than that of the Ta $3p_{3/2}$ photoelectron peak. The image contrast between Au and Ta was negligible. Thus the image in

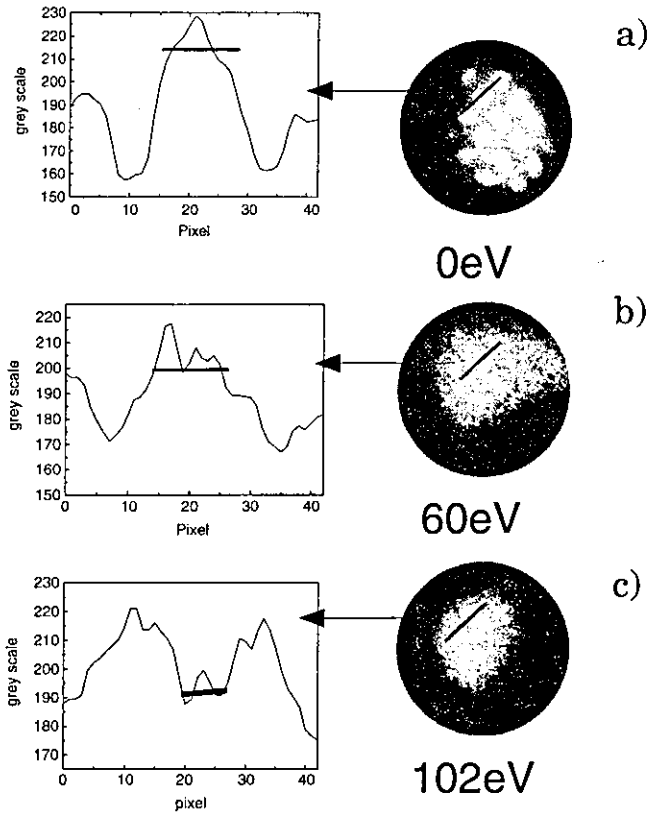

Fig. 4. Intensity plot across the Au island with photoelectron kinetic energies (a) 0 eV, (b) 60 eV and (c) 102 eV, respectively.

Fig. 3(c) was obtained using the Ta $3p_{3/2}$ photoelectrons. Figures 4(a)–4(c) show the intensity plot of the Au island. The line profile clearly indicated the contrast inversion between Fig. 4(b) and Fig. 4(c). The apparent sizes of Au islands differ between Fig. 4(a) and Fig. 4(c), which is due to the slit effect of Au islands, as mentioned above, when Ta $3p_{3/2}$ was used for imaging. The resolution estimated from Fig. 4(b) was 3–4 μm. The worse spatial resolution may be due to the limited beam time and insufficient adjustment of the lens conditions as well as the removal of the angle-limiting aperture to increase the photoelectron intensity.

In order to obtain the better imaging, we observed the same sample using an undulator beam line (BL2A). Figure 5

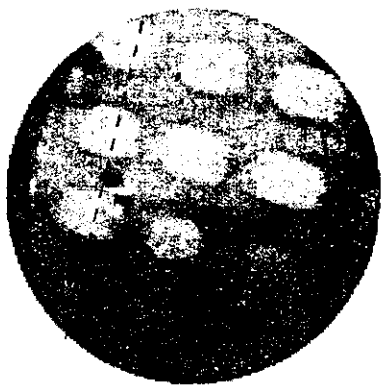

Fig. 5. Secondary electron image of Au islands on a Ta substrate using an undulator. Photon energy was 2300 eV. Selected energy was 0 eV and the energy width was 17 eV.

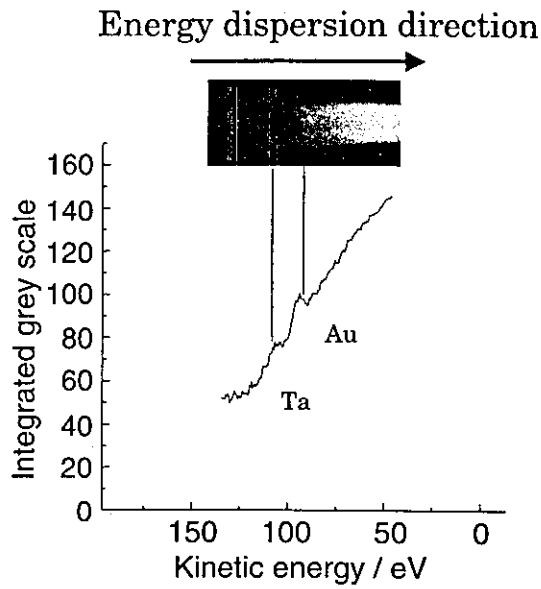

Fig. 6. Energy dispersions images (a) and intensity profile integrated over the direction perpendicular to the dispersion direction (b). Incident X-ray energy was 2300 eV. Selected energy region was 50–140 eV. Accumulation time was 10 min.

shows the secondary electron image of Au islands on Ta substrate obtained using an angle-limiting aperture and the 0 eV kinetic energy electrons. The angle limiting aperture reduced the spherical aberration and hence the sizes of the Au islands are the same as those of the real ones. The spatial resolution evaluated from the Au islands is 0.9 μm. Figure 6 shows an energy dispersion image of photoelectrons measured by using the energy dispersion mode depicted in Fig. 1(a). The kinetic energy range was 50–140 eV. The lower panel shows the intensity plot of gray scales integrated in the direction perpendicular to the energy dispersion direction. There are two peaks which correspond to Au $3d_{5/2}$ and Ta $3p_{3/2}$. Figure 7 shows the X-ray photoelectron spectra using (a) a standard hemispherical analyzer (Rigaku Co.) and (b) a Wien filter after the the background removal from the spectrum as shown in the lower panel of Fig. 6. Spectrum (a) was accumulated at BL11B with the photon energy of 2400 eV and the band-path energy for photo-

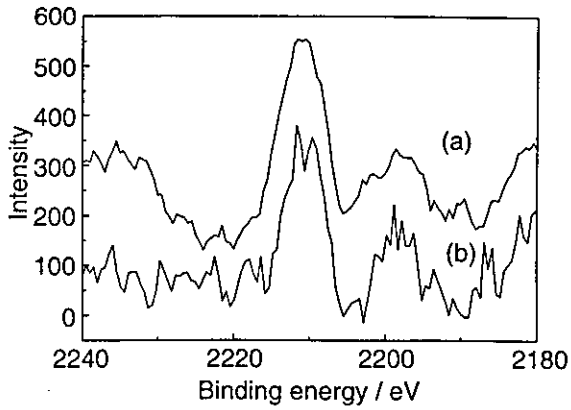

Fig. 7. Comparison of XPS spectra measured with a hemispherical energy analyzer (a) and the Wien filter energy analyzer (b).

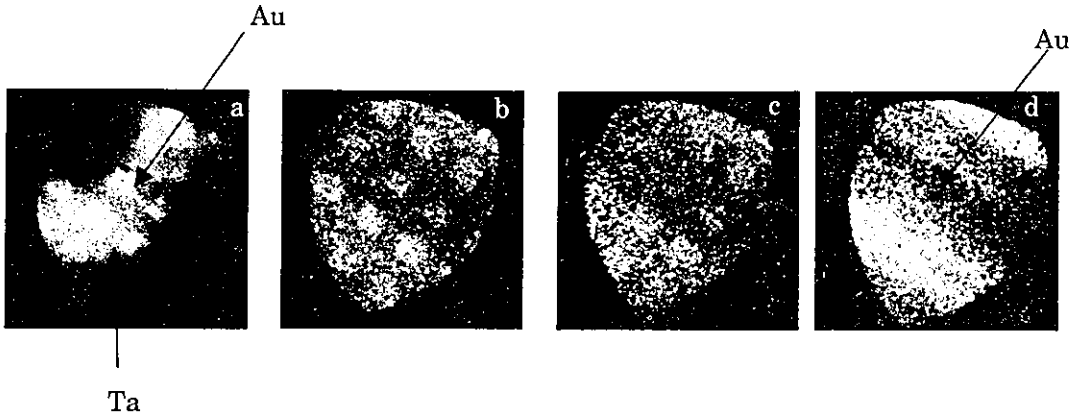

Fig. 8. Energy-filtered XPEEM images of Au on Ta substrate measured at BL2A (undulator beam line). Energy slit width corresponded to 1 eV. Kinetic energies of the images were 0 eV (a), 50 eV (b), 90 eV (c), and 102 eV (d). Photon energy was 2300 eV.

electrons to be 100 eV. There were two peaks corresponding to Au $3d_{5/2}$ and Ta $3p_{3/2}$. Peak positions were shifted in order for the Au peaks to agree with each other in Fig. 7, and to compensate for the charge up effect and the different work functions of the instruments. The peak width (FWHM = 7 eV) measured with the Wien filter was almost the same as that measured with a hemispherical analyzer, indicating that the Wien filter functioned as well as a well-established hemispherical energy analyzer.

The energy selection slit was placed after the Wien filter and it selected the photoelectron peak. The slit width corresponded to 1 eV. In order to increase the spatial resolution we set the angle-limiting aperture with an aperture size of 25 μm. The projective lens conditions were adjusted in order to obtain a real-space image as shown in Fig. 1(b). Figure 8 shows the energy-selected image. We selected the kinetic energy of photoelectrons by changing the sample bias. The selected energies were 0, 50, 90 and 102 eV. The latter two corresponded to the kinetic energies of Au $3d_{5/2}$ and Ta $3p_{3/2}$, respectively. In Figs. 8(a) and 8(b), the Au islands were brighter, as mentioned in the explanation of Figs. 3(a) and 3(b). The upper and lower regions of the images were brighter than the rest. This is due to the inhomogeneity of the incident X-ray beam intensity. The Au islands in Fig. 8(a) were smaller than those in Fig. 3(a), as we used a small angle-limiting aperture that reduced the spherical aberration. Since the amount of photoelectrons decreased significantly in the higher kinetic energy region, we needed the higher MCP voltage to amplify the contrast and longer accumulation times for the measurement of Figs. 8(c) (0.5 h) and 8(d) (6 h). Figure 8(c) showed the surface image obtained by selecting Au $3d_{5/2}$ photoelectrons: the Au islands were brighter. The picture in Fig. 8(d) was taken using Ta $3p_{3/2}$ photoelectrons. Although we required a long accumulation time (6 h), the contrast became much better than that in Fig. 3(c). In Fig. 3(c), we measured the image with the energy resolution of 15 eV, which may involve the part of Au $3d_{5/2}$. On the other hand, in Fig. 8(d), we measured the image with the energy resolution of 1 eV. Thus we could only select the Ta $3p_{3/2}$ photoelectron. Consequently we could increase the signal to background ratio and achieve a better contrast, though it took a much longer time to measure Figs. 8(c) and 8(d) than in BL11B. The spatial resolution of Fig. 8(c) was estimated to be approximately 1 μm.

The Wien filter energy analyzer has the advantage of allowing easier operation of adjustments in lens conditions owing to the collinear arrangements. Because of the low sensitivity of the analyzer, it is rarely used as an energy analyzer. However, we have demonstrated that the Wien filter energy analyzer can provide energy-selected XPEEM images. Further development in the lens and the analyzer systems will provide a brighter EXPEEM system. The objective lens using magnetic and electrostatic fields will allow higher resolution imaging of high-energy photoelectrons.[34] A Wien filter can be enlarged by removing the magnetic cores. In this case, aberrations in the Wien filter will become a serious problem. A multipole Wien filter energy analyzer offers the possibility of reducing aberrations in the energy analyzer by correcting higher order Fourier components in the aberrations.[17,18,35] By these improvements one can perform nanometer-scale chemical imaging in a reasonable time-scale and carry out EXPEEM experiments to identify the chemical interaction between the metal particles and oxide.

Finally we mention the possibility of the in-lab EXPEEM system. The photo flux we used in this study is 10^{10} photons/s at BL11B and 10^{11} photons/s at BL2A (undulator). Recent improvement of the in-lab X-ray source and optics one can get 10^{10}–10^{11} photons/s.[36,37] Therefore, it will be possible with a spatial resolution of 1 μm with the in-lab EXPEEM if one uses the present Wien-type filter EXPEEM system. If one uses an improved objective lens and an energy analyzer as mentioned above, one will achieve a spatial resolution of 100 nm or less. The in-lab EXPEEM will provide important chemical information in many material science fields such as catalyses, corrosions, electrodes and polymer surfaces.

Acknowledgement

We thank JEOL Ltd. and the Photon Factory for their technical support and Dr. H. Yoshikawa and Dr. S. Fukushima (NIMS) for their discussion. The work was financially supported by a Grant-in-Aid for scientific research (No. 11440202) and the Promotion of Joint Research and Development with Industry (Title: Develop-

ment of New XPEEM) of the Ministry of Education, Culture, Sports, Science and Technology (MEXT) and a Core Research for Evolutional Science and Technology (CREST) project of Japan Science and Technology (JST). One of the authors (H.Y.) is also financially supported by a COE project of MEXT.

1) H. H. Rotermund, W. Engel, M. Kordesch and G. Ertl: Nature **343** (1990) 355.
2) H. H. Rotermund, S. Nettesheim, A. v. Oertzen and G. Ertl: Surf. Sci. **275** (1992) L645.
3) B. P. Tonner and G. R. Harp: Rev. Sci. Instrum. **69** (1988) 853.
4) C. Ziethen, O. Schmidt, G. Fecher, C. M. Schneider, G. Schönhense, R. Froemter, M. Seider, K. Grzelakowski, M. Merkel, D. Funnemann, W. Swiech, H. Gundlach and J. Kirschner: J. Electron Spectrosc. **88–91** (1998) 983.
5) W. Swiech, G. H. Fecher, C. Ziethen, O. Schmidt, G. Schönhense, K. Grzelakowski, C. M. Schneider, R. Fromter, H. P. Oepen and J. Kirschner: J. Electron Spectrosc. **84** (1997) 171.
6) K. Siegbahn: *ESCA; Atomic, Molecular and Solid State Structure Studied by Means of Electron Spectroscopy* (Almqvist & Wiksells, Uppsala, 1967).
7) S. Gunther, B. Kaulich, L. Gregoratti and M. Kiskinova: Prog. Surf. Sci. **70** (2002) 187.
8) B. P. Tonner, D. Dunham, T. Droubay and M. Pauli: J. Electron Spectrosc. **84** (1997) 211.
9) M. zu Heringdorf, M. H. von Hoegen, T. Schmidt, E. Bauer, M. Copel and H. Minoda: Surf. Rev. Lett. **5** (1998) 1167.
10) T. Schmidt, S. Heun, J. Slezak, J. Diaz, K. C. Prince, G. Lilienkamp and E. Bauer: Surf. Rev. Lett. **5** (1998) 1287.
11) R. Wichtendahl, R. Fink, H. Kuhlenbeck, D. Preikszas, H. Rose, R. Spehr, P. Hartel, W. Engel, R. Schlögl, H. J. Freund, A. M. Bradshaw, G. Lilienkamp, T. Schmidt, E. Bauer, G. Benner and E. Umbach: Surf. Rev. Lett. **5** (1998) 1249.
12) H. Spiecker, O. Schmidt, C. Ziethen, D. Menke, U. Kleineberg, R. C. Ahuja, M. Merkel, U. Heinzmann and G. Schönhense: Nuclear Instrum. Methods A **406** (1998) 499.
13) A. Ölsner, O. Schmidt, M. Schicketanz, M. Klais, G. Schoenhense, V. Mergel, O. Jagutzki and H. Schmidt-Boecking: Rev. Sci. Instrum. **72** (2001) 3968.
14) G. Schönhense, A. Oelsner, O. Schmidt, G. H. Fecher, V. Mergel, O. Jagutzki and H. Schmidt-Boecking: Surf. Sci. **480** (2001) 180.
15) Y. Sakai, M. Kato, S. Masuda, Y. Harada and T. Ichinokawa: Surf. Rev. Lett. **5** (1998) 1199.
16) M. Kato and K. Tsuno: Nucl. Instrum. Methods A **298** (1990) 296.
17) H. Rose: Optik **83** (1987) 26.
18) M. Kato: Doctoral Thesis, The University of Tokyo (1997).
19) Y. Yamaguchi, S. Takakusagi, Y. Sakai, M. Kato, K. Asakura and Y. Iwasawa: J. Mol. Catal. **141** (1999) 129.
20) S. Takakusagi, M. Kato, Y. Sakai, K. Fukui, K. Asakura and Y. Iwasawa: J. Microsc. **200** (2000) 240.
21) H. Yasufuku, Y. Ohminami, T. Tsutsumi, K. Asakura, M. Kato, Y. Sakai, Y. Kitajima and Y. Iwasawa: Chem. Lett. (2002) 842.
22) M. Haruta: Catal. Surv. Jpn. **1** (1997) 61.
23) Y. Yuan, K. Asakura, H. Wan, K. Tsai and Y. Iwasawa: Chem. Lett. (1996) 755.
24) Y. Yuan, A. P. Kozlova, K. Asakura, H. Wan, K. Tsai and Y. Iwasawa: J. Catal. **170** (1997) 191.
25) Y. Harada, S. Yamamoto, M. Aoki, S. Masuda, T. Ichinokawa, M. Kato and Y. Sakai: Nature **372** (1994) 657.
26) S. Yamamoto, S. Masuda, H. Yasufuku, N. Ueno, Y. Harada, T. Ichinokawa, M. Kato and Y. Sakai: J. Appl. Phys. **82** (1997) 2954.
27) H. Yasufuku, M. Okumura, S. Kera, K. K. Okudaira, Y. Harada and N. Ueno: J. Electron Spectrosc. **114–116** (2001) 1025.
28) H. Yasufuku, T. Ibe, M. Okumura, S. Kera, K. K. Okudaira, Y. Harada and N. Ueno: J. Appl. Phys. **90** (2001) 213.
29) T. Tsutsumi, N. Matsudaira, H. Yasufuku, Y. Kitajima and K. Asakura: Hyomen Kagaku **24** (2003) 509.
30) S. A. Nepijko, N. N. Sedov, C. Ziethen, G. Schönhense, M. Merkel and M. Escher: J. Microsc. **199** (2000) 124.
31) S. A. Nepijko, N. N. Sedov, G. Schonhense, M. Escher, X. H. Bao and W. X. Huang: Ann. Phys. **6** (2000) 441.
32) S. A. Nepijko, N. N. Sedov and G. Schonhense: J. Microsc. **203** (2001) 269.
33) B. P. Tonner, G. E. Harp, S. F. Koranda and J. Zhang: Rev. Sci. Instrum. **63** (1992) 564.
34) H. Yoshikawa, M. Kato, Y. Sakai and S. Fukushima: Hyomen Kagaku **23** (2002) 285.
35) G. K. L. Marx, V. Gerheim and G. Schönhense: J. Electron Spectrosc. **84** (1997) 251.
36) H. Ishii, S. Shiraki, S. Omori, M. Owari, M. Doi, S. Kojima, E. Yamada, S. Takahashi, K. Tsukamoto, T. Koshikawa and Y. Nihei: *Microbeam Analysis 2000*, eds. D. B. Williams and R. Shimizu: Institute of Physics Conference Series **165** (2000) 139.
37) H. Ishii and Y. Nihei: Hyomen Kagaku **12** (2001) 774.
38) U. Johansson, H. Zhang and R. Nyholm: J. Electron Spectrosc. **84** (1997) 45.
39) J. Voss: J. Electron Spectrosc. **84** (1997) 29.
40) H. Ade, A. P. Smith, H. Zhang, G. R. Zhuang, J. Kirz, E. Rightor and A. Hitchcock: J. Electron Spectrosc. **84** (1997) 53.
41) L. Casalis *et al.*: Rev. Sci. Instrum. **66** (1995) 4870.
42) S. Gunther, A. Kolmakov, J. Kovac, L. Casalis, L. Gregoratti, M. Marsi and M. Kiskinova: Surf. Sci. **377** (1997) 145.
43) M. Kiskinova and G. Paolucci: Surf. Sci. **377** (1997) 735.

Dental Materials (2004) 20, 611-615

ELSEVIER

dental materials

http://www.intl.elsevierhealth.com/journals/dema

Rapid analysis of metallic dental restorations using X-ray scanning analytical microscopy

Motohiro Uo*, Fumio Watari

Dental Materials and Engineering, Department of Oral Health Science, Graduate School of Dental Medicine, Hokkaido University, North 13 West 7, Kita-ku, Sapporo-shi 060-8586, Japan

Received 11 November 2002; received in revised form 21 May 2003; accepted 12 August 2003

KEYWORDS
X-ray scanning analytical microscope; Elemental analysis; Fluorescent X-ray analysis; Dental alloy

Summary *Objectives.* X-ray scanning analytical microscopy (XSAM) makes it possible to analyze small specimens in air without pretreatment. The purpose of this study was to utilize XSAM for the rapid analysis of metallic dental restorations by microsampling.

Methods. Six different dental alloys were scratched with brand-new silicone points to obtain metal on the silicone point for compositional analysis. The fluorescent spectra of XSAM were measured to determine the metal attached to the specimen.

Results. The major components of the six dental metals, except for palladium, were clearly detected. The identification of palladium was difficult since the fluorescent X-ray of palladium is quite close to that of rhodium, which is the source metal of the incident X-rays. However, with a slight modification of XSAM, palladium was also identified. The total time required for sampling and analysis with XSAM was less than 10 min. The amount of the attached metal was estimated to be less than 30 μg. This amount of sampling does not damage metal restorations.

Significance. XSAM analysis using the microsampling technique is useful for the rapid analysis of metallic restorations.

Introduction

In recent years, allergies related to dental restorations have been a matter of concern.[1-3] For the identification of allergens, patch testing using diluted aqueous solutions and petrolatum of metal salts and composition analysis of metallic restorations are employed. In order to avoid functional damage to metal restorations set in the oral cavity during the analysis, a method for analyzing metal restoration without removal and damaging, is required. The microsampling method uses a silicone point and disc, and compositional analysis using X-ray photoelectron spectrometry (XPS).[4-6] This method makes it possible to analyze metallic restorations with little damage. The X-ray fluorescence spectrometer is also used for similar metal analysis.[7-9]

The recently developed X-ray scanning analytical microscope (XSAM) enables elemental mapping analysis for Na to U without pretreatment by means of energy-dispersed fluorescent X-ray spectra in air. XSAM makes it possible to obtain elemental mapping images and high-resolution X-ray transmission images.[10] The analysis is carried out in air without pretreatment even if it contains water, unlike electron probe microanalysis (EPMA)

*Corresponding author. Tel./fax: +81-11-706-4251.
E-mail address: uo@den.hokudai.ac.jp

0109-5641/$ - see front matter © 2004 Academy of Dental Materials. Published by Elsevier Ltd. All rights reserved.
doi:10.1016/j.dental.2003.08.002

and energy dispersed spectrometry (EDS) in electron microscopy which require a vacuum and electro-conductive coating. This feature is appropriate for biological specimens. The authors previously reported the application of elemental mapping analysis by XSAM for unstained soft tissue.[11-13] With a XSAM it is also possible to analyze the desired position of the specimen by monitoring with a charge-coupled device (CCD) camera. Using the microsampling technique with the silicone point, elemental analysis of the sampled point was performed simply by setting the sample in the appropriate position in a specimen chamber, aiming at the metal-attached point on the monitor and analyzing it for a few minutes. Since the whole procedure can be finished in a shorter period than for the other methods mentioned above, it is very easy and suitable for the rapid analysis of metallic restorations. Watanabe et al.[14] reported that quantitative analysis of metallic restorations could be carried from trace sample using XSAM and a scraping technique.

In this study, the fluorescence X-ray spectra from the dental metals obtained by XSAM were estimated with the aim of applying XSAM for the rapid analysis of metallic restorations by using microsampling.

Materials and methods

Sample preparation

Six different dental alloys were tested. The compositions of the alloys tested are shown in Table 1. Alloys except for amalgam were used as received. Amalgam was mixed and kept in dry air at room temperature for more than 5 years. Brand-new silicone points (type M, Shofu Inc., Kyoto, Japan) were used for the sampling of metal specimens. Metal specimens were scratched with silicone points for 2, 5 or 10 s at low revolutions (approximately 1000 rpm) and pressure (less than 10 gf) for attachment onto the silicone point. One sample was prepared for each metal specimen.

To evaluate the amount of attached metal, pure copper plate (as received) was polished under the same conditions. Silicone points with pure copper were dipped into 2 ml of 10% HCl aq. to dissolve the attached copper. The solutions were diluted to 25 ml and the concentrations were quantitated with inductively coupled plasma (ICP) analysis (P-4010, Hitachi Co. Ltd, Tokyo, Japan). The amount of attached copper was estimated from the concentration and volume of the solution.

XSAM analysis

Both metal-attached and brand-new silicone points were analyzed by XSAM (XGT-2000V, Horiba Co. Ltd, Kyoto, Japan). Incident X-rays were generated from a rhodium cathode irradiated by electrons at 50 kV, 1 mA. The X-ray guide tube (XGT) diameter, which is equal to the X-ray beam size, was 100 $\mu m\phi$ in this experiment. The parts to which metal were attached were a different color from the other parts of the silicone point, therefore it was easy to aim the XSAM camera at the metal. The fluorescent spectra were measured for 100 s for each part and each specimen was analyzed once. In the same position, a silicone point without attached metal was also analyzed to remove the background fluorescent X-rays originating from the silicone point.

Results

Metal particle attachment was easily confirmed by the change in color. The following fluorescence X-ray spectra measurements were made using metal-attached parts. The amounts of attached metal estimated using pure copper were 10, 30 and

Table 1 Compositions of alloys tested (at.%).

Product name (lot number)	System	Au	Pd	Pt	Ag	Cu	Sn	Zn	Ni	Cr	Hg
New gold-palladium[a] (0802039)	Au-Ag-Pd	6.3	19.6	-	46.2	27.8	-	-	-	-	-
18k Gold[a]	Gold alloy	55.8	-	-	12.2	32.0	-	-	-	-	-
Protor 3[b] (27697)	Gold alloy	48.9	5.2	1.8	15.5	23.3	-	5.4	-	-	-
Betalloy[c]	Ni-Cr alloy	-	-	-	-	16.1	-	-	71.1	12.8	-
Milosilver[d] (040951)	Silver alloy	-	-	-	60.1	-	16.8	23.1	-	-	-
Dispersalloy[e] (8I-710)	Amalgam	-	-	-	43.0	12.5	10.1	1.0	-	-	33.4

[a] Ishifuku Metal Co. (Tokyo, Japan).
[b] Cendres and Metaux SA (Biel-Bienne, Switzerland).
[c] Yata Dental MFG. (Osaka, Japan).
[d] GC Corporation (Tokyo, Japan).
[e] Dentsply (Pennsylvania, USA).